

Feedback from massive stars at low metallicities: MUSE observations of N₄₄ and N₁₈₀ in the Large Magellanic Cloud

A. F. McLeod,^{1,2,3*} J. E. Dale⁴, C. J. Evans⁵, A. Ginsburg⁶,
J. M. D. Kruijssen⁷, E. W. Pellegrini⁷, S. K. Ramsay⁸ and L. Testi^{8,9}

¹*School of Physical and Chemical Sciences, University of Canterbury, Science Road, Christchurch, New Zealand*

²*Department of Astronomy, University of California Berkeley, Berkeley, CA 94720, USA*

³*Physics Department, Texas Tech University, PO Box 41051, Lubbock, TX 79409, USA*

⁴*Centre for Astrophysics Research, University of Hertfordshire, College Lane, Hatfield, AL10 9AB, UK*

⁵*UK Astronomy Technology Centre, Royal Observatory Edinburgh, Edinburgh, UK*

⁶*National Radio Astronomy Observatory, Socorro, NM 87801 USA*

⁷*Astronomisches Rechen-Institut, Zentrum für Astronomie der Universität Heidelberg, Heidelberg, Germany*

⁸*European Southern Observatory, Karl-Schwarzschild-Str. 2, 85748 Garching bei München, Germany*

⁹*INAF/Osservatorio Astrofisico of Arcetri, Largo E. Fermi, 5, 50125 Firenze, Italy*

Accepted XXX. Received YYY; in original form ZZZ

ABSTRACT

We present MUSE integral field data of two HII region complexes in the Large Magellanic Cloud (LMC), N₄₄ and N₁₈₀. Both regions consist of a main superbubble and a number of smaller, more compact HII regions that formed on the edge of the superbubble. For a total of 11 HII regions, we systematically analyse the radiative and mechanical feedback from the massive O-type stars on the surrounding gas. We exploit the integral field property of the data and the coverage of the HeII λ 5412 line to identify and classify the feedback-driving massive stars, and from the estimated spectral types and luminosity classes we determine the stellar radiative output in terms of the ionising photon flux Q_0 . We characterise the HII regions in terms of their sizes, morphologies, ionisation structure, luminosity and kinematics, and derive oxygen abundances via emission line ratios. We analyse the role of different stellar feedback mechanisms for each region by measuring the direct radiation pressure, the pressure of the ionised gas, and the pressure of the shock-heated winds. We find that stellar winds and ionised gas are the main drivers of HII region expansion in our sample, while the direct radiation pressure is up to three orders of magnitude lower than the other terms. We relate the total pressure to the star formation rate per unit area, Σ_{SFR} , for each region and find that stellar feedback has a negative effect on star formation, and sets an upper limit to Σ_{SFR} as a function of increasing pressure.

Key words: HII regions – LMC – massive stars – ISM abundances

1 INTRODUCTION

Throughout their lifetime, massive stars influence their environment by injecting energy and momentum into the surrounding interstellar medium (ISM) via a series of feedback mechanisms, e.g. protostellar outflows, stellar winds, ionising radiation, supernovae (see [Krumholz et al. 2014](#) for a review). On large, kpc scales, feedback from massive stars dominates the mass and energy balance in star-forming galaxies like the Milky Way and plays a crucial role in the

evolution of galaxies by regulating the formation of new generations of stars (e.g. [Ostriker et al. 2010](#)). On smaller, <100 pc scales, massive stars are responsible for inflating HII regions, heating and ionising the surrounding gas, and adding to the turbulent velocity field of the local ISM ([Krumholz & Burkhardt 2016](#)). Qualitatively, the effect of massive stars on their environment is well understood, but a solid quantitative analysis is still missing. As a result, feedback from massive stars represents a key uncertainty in galaxy formation studies, as simulations can only reproduce the observed galaxy population by tuning the strength of stellar feedback ([Schaye et al. 2015](#), [Vogelsberger et al. 2014](#)).

* E-mail: anna.mcleod@canterbury.ac.nz

Giant HII regions and super-bubbles around massive stars and star clusters are among the most prominent features of star-forming galaxies. Their evolution links stellar feedback from the small to large scales, as they are believed to represent evolved HII regions, the expansion of which is driven by stellar winds and supernovae Oey (1996c). However, to understand and evaluate the role stellar feedback plays in driving the dynamics of these regions, it is imperative to characterise the massive stellar content within them. The past two decades have seen many studies tackle feedback, ionisation structures, morphologies, dynamics and stellar content of feedback-driven bubbles and HII regions (e.g. Lopez et al. 2014, Lopez et al. 2011, Pellegrini et al. 2011, Pellegrini et al. 2010, Oey 1996b, Oey 1996a, among many others), in an ever-increasing effort aimed at disentangling and observationally quantifying the impact of the various feedback mechanisms.

Optical integral field spectroscopy (IFS) is ideally suited to analyse both the gaseous (McLeod et al. 2016a, Kehrig et al. 2016, McLeod et al. 2015, Monreal-Ibero et al. 2011) and stellar (Castro et al. 2018, Zeidler et al. *in press*) components of Galactic and nearby extragalactic HII regions. The advantage of IFS over conventional imaging or spectroscopy is the fact that it combines both, which allows the simultaneous derivation of kinematics and physical quantities of the feedback-driving stars and feedback-driven gas with the same data set. The power of IFS data to link the massive stellar population to feedback-driven structures in HII regions has been demonstrated in McLeod et al. (2016b), where we showed a tight correlation between the rate at which molecular cloud structures are photo-evaporated by stellar feedback, and the amount of ionising photon flux originating from the nearby O-type stars.

In this work, we exploit optical integral field data from the MUSE instrument mounted on the Very Large Telescope (VLT), to analyse the properties and kinematics of the ionised gas in two HII region complexes in the Large Magellanic Cloud (LMC), and connect these to the populations of massive, feedback-driving O-type stars that have formed in the two regions. The LMC is an ideal target for stellar feedback studies, as it is nearly face on (hence allowing a convenient viewing angle); it hosts numerous massive star-forming regions; it does not suffer from the heavy extinction we would face if observing Galactic HII regions; at 50 kpc, it is at an ideal distance to observe entire regions within a feasible amount of telescope time and yet still be able to resolve and classify individual stars. Furthermore, the LMC is characterised by a lower metallicity (~ 0.5 solar), a lower dust-to-gas ratio (Roman-Duval et al. 2014), and a corresponding environment in which the effect of ionisation is enhanced (Israel et al. 1986) and the impact of radiation pressure subdued, therefore allowing one to probe stellar feedback in a lower-metallicity environment.

As part of a pilot program to map HII regions in the Magellanic Clouds with MUSE we obtained $8' \times 8'$ mosaics of the giant HII regions N44 (DEM L152) and N180 (DEM L326). Both regions consist of a central, giant bubble, on the rim of which smaller and more compact HII regions have formed. Because of the large number of targeted HII regions of different sizes and morphologies, these two targets offer a superb opportunity of investigating stellar feedback for a multitude of stellar contents and bubble parameters with

just two data sets. N44 is one of the most luminous HII regions in the LMC after 30 Doradus, it contains 3 OB associations (LH 47, 48 and 49, Lucke & Hodge 1970), and it is associated with a supernova remnant located about 6 arcminutes NE of the main central bubble. N44 seems to be more massive and more evolved than N180: Oey & Massey (1995) classify >30 O-type stars, and find evidence for two episodes of star formation, an earlier (~ 10 Myr) episode which occurred inside the main bubble, and a later (~ 5 Myr) episode outside of the latter. N180 hosts the young (<10 Myr, Bica et al. 1996) cluster LH 117 (Lucke & Hodge 1970) which contains several O-type stars, as well as over 30 young stellar objects (Caulet et al. 2008).

This paper is organised as follows: Section 2 describes the observations, data reduction and calibration; in Section 3 we proceed in spectroscopically and photometrically identifying and classifying the massive stellar content of N44 and N180; following this, we characterise the two HII regions in terms of their luminosities, morphologies, sizes, densities, ionisation structure and kinematics in Section 4; in Section 5 we combine the information about the feedback-driving massive stars and the feedback-driven gas to analyse the radiative and mechanical feedback, and discuss photon leakage in Section 6; finally, we discuss (Section 7) and summarise (Section 8) our findings.

2 OBSERVATIONS

All observations were taken with the integral field spectrograph MUSE (Bacon et al. 2010) mounted on the VLT under the program 096.C-0137(A) (PI McLeod). In the Wide Field Mode used for this program, MUSE has a pixel scale of 0.2 arcsec/pixel, a resolving power of 1770 to 3590 (from 4750 to 9350 Å), and a spectral separation of 1.25 Å between single frames. Both HII regions were observed with a 64-pointing mosaic, spanning a total size of 8×8 arcminutes. Each pointing was observed twice in a 90° rotation dither pattern with an integration time of 90 seconds per exposure. Each mosaic therefore consists of 128 single telescope pointings. The observations were scheduled into 1-hour observing blocks of 16 pointings each. Hence, the mosaics are divided into 8 horizontal stripes of 8 final data cubes, where each of the stripes corresponds to one observing block. Due to the filler nature of this program, different observing blocks were executed on different dates with widely varying observing conditions. The consequence of a lower seeing-limited spatial resolution due to the poor observing conditions is still noticeable as can be seen in Fig. 1, where the lower-quality observing blocks results in the stripy nature of the image. We will discuss the effect of this on the analysis in the following sections.

The data was reduced using the MUSE pipeline (Weilbacher et al. 2012) under the ESOREX environment and the standard static calibration files which come with the installed pipeline. For each observing block we used the available calibration files from the ESO archive for the relevant night. The resulting two data cubes of each pointing (one per 90° rotation telescope pointing) were then combined into a final data cube by using the built-in exposure alignment and combination package of the MUSE pipeline.

We proceeded in the same manner as with our previous

Emission line	λ_{cen} (continuum) Å
H β	4945
OIII λ 5007	5035
H α , [NII] λ 6584	6617
SII λ 6717,31	6760
OII λ 7320,30	7210

Table 1: Central wavelengths of the spectral extraction (width = 6 Å see text Section 2) used to produce the continuum maps from the MUSE data cubes.

MUSE programs and analyses (McLeod et al. 2015, 2016a,b) in producing extinction-corrected maps of the main nebular emission lines, velocity maps, and electron density maps. We exploit the wavelength coverage of MUSE to compute extinction maps via the Balmer decrement for the entire observed mosaic of both regions. For this, we use PYNEB (Luridiana et al. 2015) and assume an extinction curve for the LMC as in Gordon et al. (2003). Fig. 1 shows three-colour composites obtained from the extinction-corrected [SII] λ 6717 (red), H α (green) and [OIII] λ 5007 emission line maps. To highlight both the morphology of the gas and the location of the feedback-driving stars, the maps in Fig. 1 are not continuum-corrected. For the nebular emission line maps of interest in this paper (H α , H β , [SII] λ 6717,31, [NII] λ 6584, [OIII] λ 5007) we produce continuum maps from a portion of the spectrum close to the relevant lines which does not show any kind of line structure (nebular emission lines or sky lines), by using the same spectral width used to compute the emission line maps (namely ± 3 Å around the lines of interest, as summarised in Table 1). We subsequently subtract the continuum maps from the emission line maps. We note that the continuum subtraction of this emission line map leads to negative values where stellar emission is over-subtracted. In the extinction correction procedure, negative values are set to nan values, and because the dereddening is based on the H β map, the pixels with nan values are propagated to the other emission line maps. This leads to apparent stellar emission at the locations of the stars in the electron density map (see Section 4.2), where nan values are interpolated over during the smoothing procedure.

To test the performance of the data reduction and flux calibration we compare the MUSE data to archival H α narrow-band data from the SHASSA¹. Comparing MUSE fluxes to other narrow-band optical data requires mimicking said narrow-band filters with the MUSE cube. Hence, we make an emission line map from the MUSE data by summing the flux in the frames contained in the filter specifications of the SHASSA data, corresponding to a 32 Å wide filter centred on the H α line. We then perform aperture photometry² on the MUSE and SHASSA maps on circular apertures with a 3.85' radius centred on the two regions (5:48:49.46 -70:03:19.53 and 5:22:08.13 -67:56:08.26 for N180 and N44 respectively). We estimate errors on the aperture fluxes by providing an error map to the aperture photometry routine, obtained by assuming a generous 25% error on the flux of the emission line maps. Table 2 shows the

N44	
F _{MUSE}	F _{SHASSA}
6.99 \pm (6 \times 10 ⁻⁴)	7.21 \pm 0.10
N180	
F _{MUSE}	F _{SHASSA}
4.64 \pm (5 \times 10 ⁻⁴)	4.50 \pm 0.06

Table 2: Comparison of the H α fluxes obtained from the MUSE data set presented in this work, and from archival SHASSA data (Gaustad et al. 2001). Fluxes are obtained by performing aperture photometry on circular regions and are in units of 10⁻¹⁰ erg cm⁻¹ s⁻², and are pre-extinction correction.

result of the comparison: the two datasets agree within 5% of flux values, and we are therefore confident of the reduced data products.

3 CHARACTERISATION OF THE MASSIVE STELLAR CONTENT

To compare the HII regions in terms of their morphologies, kinematics, ionisation diagnostics and feedback characteristics described in the following sections, it is necessary to first understand and characterise their massive stellar content. We exploit the MUSE IFS data to identify and classify the massive O-type stars based on a method consisting of the following steps³:

- (i) spectra of the brightest ($m_V < 21$) objects are extracted from all of the 64 individual MUSE cubes available per region;
- (ii) the spectra of the sources identified in (i) are cropped to a relevant portion around HeII λ 5411 line ($\lambda_{\text{min}} = 5350$ Å, $\lambda_{\text{max}} = 5500$ Å), the continuum is fitted and subtracted, and the level of noise N is determined as the standard deviation of the continuum;
- (iii) stars are flagged as O-type if within $\sim \pm 15$ Å of the HeII line (5400 - 5430 Å) we find at least 2 data points larger than $3.5N$ to determine the presence of the absorption line; $3.5N$ was chosen as a reference value, given that a lower limit results in a large number of false positive detections, while a higher limit yields a large number of non-detections;
- (iv) the spectra flagged as O-type are then inspected by eye to check the performance and validity of the HeII line identification routine;
- (v) the equivalent width (EW) of the HeII λ 5411 and HeI λ 4922 absorption lines in the spectra of the visually confirmed O-stars are computed; here, we fit the absorption lines with Gaussian, Lorentzian and Voigt profiles, and use the best fitting model based on χ^2 -minimisation;
- (vi) the ratio of the EWs of the two lines ($R = \text{EW}_{4922}/\text{EW}_{5411}$)

³ A public release of the automated O-star detection and classification from MUSE data is planned for the near future, which will be followed by an automated general spectroscopic classification algorithm. To obtain more information, please contact the lead author.

¹ Southern H α Sky Survey Atlas, Gaustad et al. 2001.

² For this we use the Photutils package, <http://www.astropy.org>

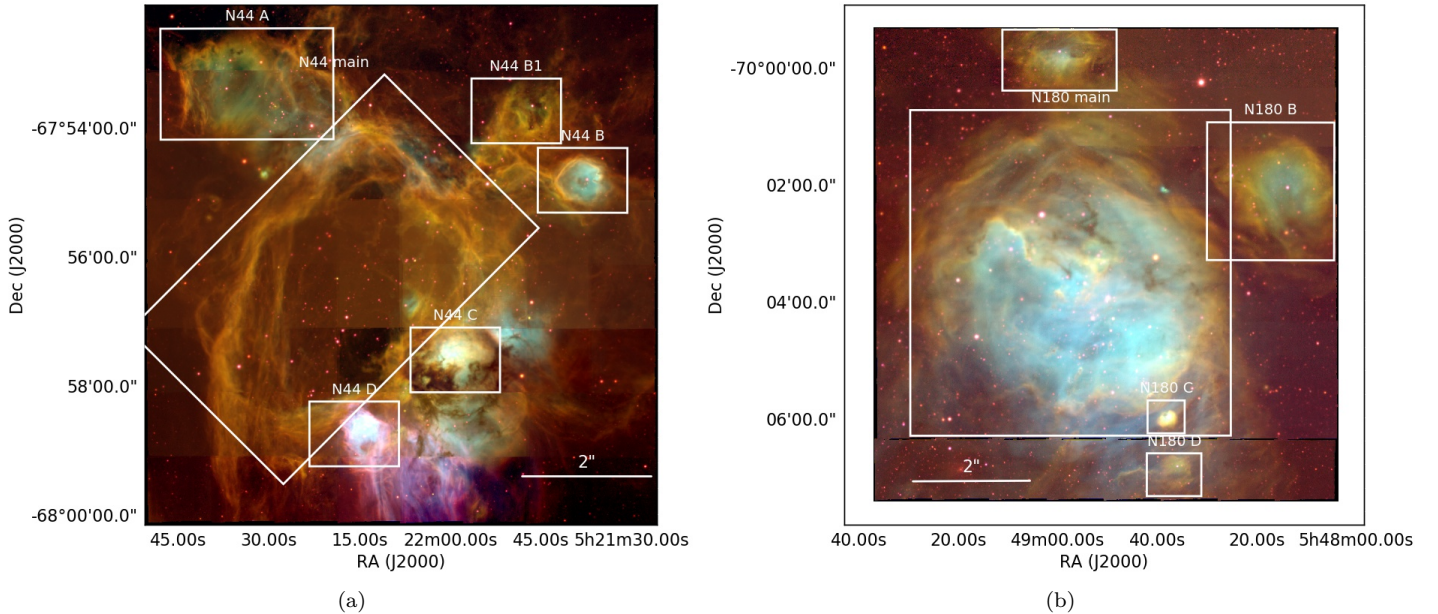


Figure 1. Three-colour composites of N44 (a) and N180 (b). Red corresponds to [SII] λ 6717, green to H α , and blue to [OIII] λ 5007 (stretched logarithmically). Here and in all following figures north is up and east is left. Suboptimal observing conditions during the observations of N44 lead to lower spatial resolution in three observing blocks. The sub-regions analysed in this work are marked in white.

is then used to determine the spectral type according to the empirical relations given in [Kerton et al. \(1999\)](#);

- (vii) finally, we perform aperture photometry on the collapsed (i.e. summed) portion of the cube covering the Johnson-Cousins V band ($\sim 4950 - 6050 \text{ \AA}$), and with a distance of 50 kpc to the LMC and a mean extinction towards the LMC of $A_V \sim 0.38 \text{ mag}$ ([Imara & Blitz 2007](#)), we obtain absolute magnitudes M_V for the O stars, and infer the luminosity class of the stars according to [Martins et al. \(2005\)](#).

The source identification in step (i) is performed with dendrograms⁴. The dendrogram pruning settings are chosen such that faint ($m_V > 21$) sources are automatically ignored. This does not lead to any losses in terms of unidentified O-type stars (at the distance of the LMC this magnitude cut corresponds to an absolute magnitude of $M_V = 2.5$, where late-type O stars have $M_V \sim -3.9$ and brighter). Finally, for each star we determine the ionising photon flux $Q_{0,*}$ (in photons/s) according to the calibrations given in [Martins et al. \(2005\)](#). For the purpose of this work we limit our analysis to O-type stars, which dominate in terms of ionising photon flux. N44 and N180 have 24 and 6 known B-type stars ([Skiff 2014](#)), respectively, and with an indicative flux of $\log(Q) \sim 48 \text{ s}^{-1}$, this amounts to only about 10% and 5% of the respective integrated values for the O star population. For the magnitudes derived as per step (vii), we find mean errors of ± 0.019 and ± 0.016 for all stars in N44 and N180, respectively.

The classification method used here comes with a series of potential caveats, which we now briefly discuss. One assumption was that of the assumed distance and extinction on which the estimate of the luminosity class is based. Most

of our stars have published $B - V$ colours in the references listed in Tables 3 and 4. These are typically $-0.1-0.2 \text{ mag}$, so consistent with our assumed extinction above. In a couple of cases (LH117-98 and LH117-144) $B - V \sim 0.00 \text{ mag}$, implying an extinction of $\sim 1 \text{ mag}$ (assuming $B - V_0 = -0.3$ for an O-type star). LH47-182 is the furthest outlier, with $B - V = 0.13 \text{ mag}$, resulting in $A_V \sim 1.5 \text{ mag}$. Compared to the calibrations from [Martins et al. \(2005\)](#) these three stars should still be robust to within one luminosity class, sufficient for our study of stellar feedback. A follow-up study of the entire stellar populations of N44 and N180 (down to the observational limit) with a classification based on stellar parameters is planned for the near future. Next, line infilling from strong nebular emission could lead to classifications towards earlier spectral types, and hence an overestimate of $Q_{0,*}$. We do not expect this to be a major issue for N44 and N180, as HeII λ 4922 is prone to nebular contamination only for exceptionally strong nebular emission. Similarly, wind contamination of the HeII λ 5411 is only problematic in the case of extreme supergiants, which we do not observe here. Finally, we note that to be confidently distinguished from early-type B stars, O9.5 and O9.7 stars ideally need additional diagnostics (e.g. SiIII and NII lines).

The identified O-type stars are listed in Tables 3 and 4, together with their coordinates, their derived spectral types and inferred luminosity classes, apparent magnitudes, photon fluxes and radial velocities (determined from the HeII lines). For the last two we list values obtained from this work, and where available, we also list the spectral type found in literature. Our sample appears to be complete in terms of correctly identifying stars already classified in previous studies. We also identified 10 previously unknown O-type stars (five per region). In the following two subsections we will describe the O-star identification process and the classified objects for N44 and N180 separately.

⁴ Astrodendro (<http://www.dendrograms.org/>)

3.1 O-type stars in N44

In terms of number of O stars, N44 is the more populous of the two analysed regions. Past studies (Will et al. 1997, Oey & Massey 1995, Conti et al. 1986, Rousseau et al. 1978) have already classified a total of 34 O stars within the region covered by our MUSE observations. As already mentioned in the introduction, in addition to having formed more stars, N44 appears to be slightly older than N180 when it comes to the stellar population. Furthermore, it hosts the evolved Wolf-Rayet star WN4b (Hainich et al. 2014), located in N44 main (see Fig. 1 concerning the nomenclature of the various subregions). For this class of Wolf-Rayet stars, Crowther (2007) give a Lyman continuum ionising flux of $\log(Q_{HI}) \sim 49.2 \text{ s}^{-1}$.

From the MUSE data we are able to correctly identify 33 of the 34 literature stars, while LH 47-14, classified as an O9.5 V star in Oey & Massey (1995), has been reclassified as a class B star in this work based on both the HeII and HeI EWs (0.29 and 0.79, respectively). Out of the identified O stars, 10 clearly lie within the bubble that is N44 main (see Fig. 2a). N44 A in the NE corner of the FOV contains 3 O stars, two known and a newly classified one. N44 B, B1 and D all contain a single O star each, out of which the O5 V source in N44 D is the most luminous one (correspondingly, N44 D is one of the brightest regions in N44). N44 C hosts 3 O stars, among which LH 47-191 is the most luminous in the entire observed region. The remaining O stars are scattered around the main bubble and the smaller surrounding HII regions, some do not appear to be associated with nebulosities. Where these concentrate in (at least projected) groups, smaller ionisation fronts are identified (e.g. just NW of N44 C, and at the top of N44 main). The summed photon flux of all O-type stars in N44 amounts to $\log(Q_{0,*}) \sim 50.40 \text{ s}^{-1}$ (including the WR star). Despite being one of the brightest regions in the LMC, this is an order of magnitude less than the flux emitted by R136 in 30 Doradus (Crowther & Dessart 1998), and almost 4 times weaker than the flux in NGC 3603 (one of the most massive star-forming regions in the Milky Way, McLeod et al. 2016b). Spectra of all identified stars are shown in Appendix B.

In Table 3 a number of stars are listed for which the magnitudes derived from the MUSE data are consistently lower than literature values. This is true for all (and only) stars in observing blocks 4 and 5 which suffered from the worst observing conditions. Hence, for these stars, we use the apparent magnitude from literature.

3.2 O-type stars in N180

In the central bubble (N180 main) we expect to find 14 O-type stars (Massa et al. 2003, Smith Neubig & Bruhweiler 1999, Massey et al. 1989, Conti et al. 1986). Our algorithm correctly extracted and identified 13 of these as O stars, while one of them, LH 117-19, was not flagged as an O star and inspection of the spectrum confirms the absence of the HeII λ 5411 absorption line. We therefore suggest that LH 117-19 is an early-type B, rather than an O star. The spectra of the 13 identified N180 main stars, cropped around the HeII and HeI lines, are shown in Appendix B, Fig. B3 and Fig. B4, respectively. Fig. B3(a) shows the clear detection of the HeII line for the brightest O stars in the main bubble,

and Fig. B4(a) illustrates the weakness of the HeI line as a consequence of the early spectral type for the four most luminous stars (LH 117-43A, LH 117-98, Sk-70 115 and LH 117-214). For these four objects, the spectral type was determined with the EW of the HeII line only, according to Eq. 2 in Kerton et al. (1999) rather than based on the ratio of the two. The brightest star in N180 is LH 117-214, an O3 V star, located towards the south-western rim of N180 main. We also detect the two previously classified stars south-east of the main bubble, LH 118-165 and LH 118-182. These do not appear to be associated with N180, nor with ionised gas in their vicinity, and their radial velocities suggest them as large-amplitude binaries. We therefore do not include these in subsequent analyses, but list them in Table 4 for completeness.

In addition to the identification of already known stars, we expand the census of O-type stars in N180 by a total of five newly classified objects (see Fig. 2b). Of these, MUSE N180-1 (a late-type O star) resides within N180 main; MUSE N180-2 is associated with the smaller HII region N180 A north of the main bubble; MUSE N180-4 is associated with N180 B; and finally MUSE N180-5 is driving the small, compact region N180 C immediately south of N180 main. As discussed in Section 5, the surrounding smaller HII regions have radii of the order of 10 to 40 times smaller than the main bubble. The brightest and smallest of these is N180 C, which spans about 6 pc in diameter and contains an O8.5 V star. N180 D contains what is either a late O star or an early B star which displays a very weak HeII line. This star, if of spectral type O, is a false negative of our identification algorithm, as it only has one data point larger than the noise around the line, and thus does not satisfy our selection criterium. Together with an absolute magnitude of $M_V \sim -3.98$, we therefore suggest that this star is an early-type B star rather than a late O star, and assign it a tentative spectral type B0.5 III (Wegner 2006), and from Sternberg et al. (2003), this translates to $\log(Q_{0,*}) = 48.06 \text{ s}^{-1}$. We therefore do not list it in Table 4, but given that it appears to be associated with a small HII region where no O star is found, we still include it in the analysis of the following sections. The summed photon flux of all O-type stars identified in the N180 mosaic is $\log(Q_{0,*}) \sim 50.12 \text{ s}^{-1}$.

4 CHARACTERISATION OF THE HII REGIONS

4.1 Sizes and morphologies

The two regions display different morphologies on about the same physical scales (Fig. 1). Apparent sizes of the various subregions in the two complexes are determined from radial flux profiles, such that the size of a bubble is given by the radius R_{90} which encompasses 90% of the measured H α flux. The main physical parameters for each region are listed in Table 5, and Fig. D1 and D2 show the radial profiles, together with the limiting radius, for each subregion.

N44 (DEM L152), located about 1.8° NW of 30 Doradus, consists of a superbubble (N44 main, see Fig. 1) seemingly devoid of ionised gas, along the rim of which several more compact HII regions are located. N44 main is roughly elliptical with a major axis (which has a P.A. of 37° west

Star	R. A. (J2000)	Dec. (J2000)	Spectral Type Literature	Reference	EW _{HeI} ^a	EW _{HeI} ^a	Spectral Type ^b (this work)	<i>m</i> _V	<i>m</i> _V .MUSE	log(Q _{0,*}) _{s-1}	<i>v</i> _r km s ⁻¹	Notes
LH 48-9	05 22 37.13	-67 53 32.8	O7 III	Conti et al. (1986)	0.89	0.28	O7 III	13.50	13.46	49.13	306.82	N44 A
LH 48-65	05 22 13.48	-67 53 38.2	O9 III	Oey & Massey (1995)	0.49	0.35	O8.5 I	12.92	12.81	49.19	300.07	
LH 48-4	05 21 54.95	-67 53 53.5	O9 V	Oey & Massey (1995)	0.48	0.62	O9.5 III	14.24	14.01	48.42	299.85	
Sk-67 83	05 21 50.44	-67 53 13.6	Bo.5 III	Massey et al. (1995)	0.47	0.55	O9.5 III	13.10	13.07	48.42	300.25	N44 B1
Sk-67 82	05 21 46.76	-67 53 38.1	Bo.5	Rousseau et al. (1978)	0.59	0.62	O9 III	13.20	13.07	48.65	321.16	
LH 48-111	05 22 21.61	-67 54 08.9	O5 V((**))	Oey & Massey (1995)	1.17	-	O5 V	14.43	14.41	49.22	308.69	weak HeI, N44 A
LH 48-33	05 22 04.19	-67 54 28.1	O8 V	Oey & Massey (1995)	0.57	0.47	O8.5 V	14.23	14.15	48.27	260.34	
LH 48-14	05 21 58.44	-67 54 28.0	O8.5 V	Oey & Massey (1995)	0.63	0.53	O8.5 V	14.13	14.13	48.27	330.50	
LH 48-28	05 22 02.71	-67 54 22.8	O9 V	Oey & Massey (1995)	0.53	0.57	O9 V	14.20	14.21	48.06	278.94	
LH 48-26	05 22 01.86	-67 54 16.6	O9.5 V	Oey & Massey (1995)	0.60	0.43	O9.5 V	14.09	14.08	47.88	286.69	
[WBD97] N44 6	05 21 37.65	-67 54 48.5	O8 III	Will et al. (1997)	0.88	0.42	O8 III	13.40	13.37	48.88	295.72	N44 B
LH 47-275	05 22 07.31	-67 56 04.2	O8.5 V	Oey & Massey (1995)	0.51	0.43	O8.5 V	13.88	(14.15)	48.27	311.69	main
[WBD97] N44 3	05 22 03.79	-67 55 28.8	Bo.5 Iab	Will et al. (1997)	0.24	0.61	O9.5 I	12.60	(13.97)	49.00	306.76	main, use HeI only
LH 47-47	05 21 47.34	-67 55 40.8	O9.5 V	Oey & Massey (1995)	0.20	0.58	O9.5 V	13.49	(13.97)	47.88	264.78	clear HeI
LH 47-407	05 22 20.57	-67 56 48.3	O9.5 V	Oey & Massey (1995)	0.28	0.64	O9.5 V	13.84	(14.25)	47.88	309.30	main
LH 47-320	05 22 11.87	-67 56 41.1	O9.5 V	Oey & Massey (1995)	0.41	0.58	O9.5 V	14.47	(15.07)	47.88	295.14	main
[WBD97] N44 7	05 22 07.49	-67 56 45.7	O9 III	Will et al. (1997)	0.77	0.21	O7 III	13.40	(14.20)	49.13	321.35	main
[WBD97] N44 4	05 21 57.87	-67 56 25.6	O7 III	Will et al. (1997)	0.67	0.19	O6.5 III	13.00	(13.85)	49.23	315.61	main
LH 47-222	05 22 02.63	-67 56 23.9	O8 V	Oey & Massey (1995)	1.36	0.51	O7.5 V	14.71	(14.97)	48.61	311.36	main
LH 47-138	05 21 57.06	-67 56 59.6	O8.5 V	Oey & Massey (1995)	0.73	0.53	O8.5 V	14.29	(14.89)	48.27	319.86	
LH 47-66	05 21 49.17	-67 56 50.0	O9 V	Oey & Massey (1995)	0.56	0.37	O8 V	14.65	(15.29)	48.44	297.13	
LH 47-58	05 21 48.24	-67 56 22.4	O9.5 III	Oey & Massey (1995)	0.16	0.72	O9.5 III	14.10	(14.83)	48.42	312.90	use HeI only
LH 47-433	05 22 22.74	-67 58 05.8	O9.5 V	Oey & Massey (1995)	0.47	0.56	O9 V	14.15	14.25	48.06	306.25	main
LH 47-402	05 22 20.39	-67 57 48.1	O6.5 V((f))	Oey & Massey (1995)	0.97	0.33	O7 V	14.41	14.44	48.75	314.33	main
[WBD97] N44 5	05 22 17.81	-67 57 09.2	O9 III	Will et al. (1997)	0.49	0.41	O8.5 III	13.30	13.38	48.75	290.00	main
LH 47-277	05 22 07.49	-67 58 02.9	O9.5 V	Oey & Massey (1995)	0.48	0.68	O9.5 V	15.04	14.93	47.88	293.27	main
LH 47-191	05 21 59.75	-67 57 36.7	O5 III(f)	Oey & Massey (1995)	0.92	0.09	O5 III	14.14	13.49	49.48	301.30	N44 C
[WBD97] N44 12	05 21 59.53	-67 57 21.1	O8 V	Will et al. (1997)	0.86	0.46	O8 V	13.90	13.85	48.44	359.42	N44 C
LH 47-131	05 21 56.59	-67 57 33.7	O9.5 V	Oey & Massey (1995)	-	0.64	O9.5 V	15.23	15.09	47.88	241.05	weak HeI, N44 C
LH 47-71	05 21 49.84	-67 57 07.6	O6 V((f))	Oey & Massey (1995)	1.07	-	O5 V	15.34	15.53	49.22	317.70	no HeI
LH 47-15	05 21 43.56	-67 57 08.7	O9 V	Oey & Massey (1995)	0.68	0.31	O7.5 V	14.26	14.38	48.61	298.85	
LH 47-338	05 22 13.92	-67 58 37.3	O7 V((f))	Oey & Massey (1995)	1.16	-	O5 V	14.20	13.61	49.22	274.11	no HeI, N44 D
LH 47-182	05 21 59.00	-67 58 34.8	O6 V((f))	Oey & Massey (1995)	1.20	0.17	O5.5 V	14.56	14.21	49.10	255.32	
MUSE N44-1	05 21 50.04	-67 52 24.1	-	-	0.58	0.48	O8.5 III	-	13.77	48.75	311.11	field?
MUSE N44-2	05 22 29.93	-67 54 02.6	-	-	0.90	0.57	O8 V	15.10 ^c	14.76	48.44	304.12	(N44 A)
MUSE N44-3	05 21 47.90	-67 54 54.7	-	-	0.65	0.53	O8.5 V	14.45 ^c	14.35	48.27	352.68	
MUSE N44-4	05 21 53.81	-67 54 09.5	-	-	0.45	0.49	O9 V	14.41 ^c	-	48.06	307.82	
MUSE N44-5	05 22 09.36	-67 58 31.2	-	-	0.70	0.90	O9.5 V	-	15.23	47.88	312.94	

^aSeveral spectra, especially the HeII lines of the early-type sources, show clear Lorentzian-shaped absorption lines, while others display Gaussian or Voigt profiles. The displayed values are obtained from applying the closest matching distribution, determined via χ -square fitting.

^bSpectral types from the ratio of the HeI λ 922/HeII λ 5411 lines (Kerton et al. 1999). Adopted luminosity classes are inferred on the basis of the estimated absolute magnitudes for each star, cf. the models of Martins et al. (2005).

^cfrom Zaritsky et al. (2004).

Table 3: O stars identified in N44. Unless specified, literature magnitudes are taken from the cited reference. Apparent magnitudes in parenthesis correspond to stars in the two observing blocks with the worst observing conditions. For these, we use the literature *m*_V value. Radial velocities are determined from the HeII line.

Star	R. A. (J2000)	Dec. (J2000)	Spectral Type literature	Reference	EW _{HeII} ^a	EW _{HeI} ^a	Spectral Type (this work)	<i>m</i> _V	<i>m</i> _V (this work)	log(<i>Q</i> _{0,*}) s ⁻¹	<i>v</i> _r km s ⁻¹	Notes
LH 117-43	05 49 09.09	-70 03 05.20	O6 V	Massey et al. (1989)	1.12	0.29	O6.5 V	14.08	14.09	48.88	238.82	
LH 117-62	05 48 51.63	-70 03 12.10	O9 V	Massey et al. (1989)	0.46	0.55	O9 V	14.75	14.56	48.06	212.58	
LH 117-14	05 48 54.62	-70 02 29.80	O6.5((f))	Massey et al. (1989)	0.87	-	O6.5 V ^b	14.69	14.65	48.88	66.62	no HeI
LH 117-103	05 49 19.51	-70 03 37.30	O9.7	Massey et al. (1989)	0.10	0.29	O9.5 III - Bo III	13.53	13.94	48.42 ^c	167.77	weak F
LH 117-43A/140	05 48 52.67	-70 04 16.42	O3 III((f*)) - O4((f*))	Massey et al. (1989)	1.09	-	O5 V ^b	13.52	13.54	49.22	231.30	weak F
LH 117-98	05 48 57.64	-70 03 34.10	O9	Massey et al. (1989)	-	-	-	14.94	14.81	48.06	213.2	literatu
Sk-70 115	05 48 49.65	-70 03 57.82	O6.5 Iaf	Massa et al. (2003)	0.72	-	O7.5 I	12.17	12.26	49.31	278.51	weak F
LH 117-144	05 48 30.85	-70 04 18.50	O9	Massey et al. (1989)	-	0.60	O9.5 V - Bo V	15.23	15.05	47.88 ^c	294.05	weak F
LH 117-183	05 48 54.56	-70 04 56.70	O9	Massey et al. (1989)	0.64	0.74	O9.5 V	14.24	14.95	47.88	287.22	
LH 117-13	05 48 39.03	-70 04 58.60	O8 V	Smith Neubig & Bruhweiler (1999)	0.59	0.48	O8.5 V	15.14	14.49	48.27	225.8	
LH 117-214	05 48 48.72	-70 05 32.20	O3/4	Massey et al. (1989)	1.33	-	O3 V	13.15	13.29	49.64	224.38	no HeI
LH 117-206	05 48 42.02	-70 05 22.80	O8	Massey et al. (1989)	0.88	0.46	O8 V	15.06	14.85	48.44	242.43	
LH 117-16	05 48 41.22	-70 04 27.70	O7 V	Conti et al. (1986)	0.62	0.44	O8 V	14.04 ^d	13.96	48.44	271.04	
MUSE N180-1	05 48 48.97	-70 04 45.80	-	-	0.49	0.66	O9.5 V	15.75 ^d	15.36	47.88	257.59	
MUSE N180-2	05 48 59.53	-69 59 43.80	-	-	0.85	0.39	O7.5 V	14.86 ^d	14.52	48.61	232.95	N180 I
MUSE N180-3	05 48 49.06	-70 00 50.85	-	-	0.65	0.54	O8.5 V	14.48	14.75 ^d	48.27	231.47	
MUSE N180-4	05 48 13.70	-70 02 04.31	-	-	0.82	0.29	O7 III	13.92 ^d	13.85	49.13	241.50	N180 I
MUSE N180-5	05 48 37.94	-70 05 58.20	-	-	0.60	0.46	O8.5 V	15.95 ^d	15.54	48.27	223.17	N180 C
LH 118-105 ^f	05 49 30.62	-70 06 04.10	O9	Massey et al. (1989)	-	0.66	O9.5 V	15.15	14.93	47.88	77.76	weak F
LH 118-182 ^f	05 49 21.37	-70 06 29.80	O9III	Massey et al. (1989)	0.43	0.60	O9.5 III	13.78	13.84	48.42	62.66	
MUSE N188-6 ^g	05 48 35.83	-70 06 48.0	-	-	0.13	0.99	Bo.5 III	14.79 ^d	14.89	48.06	263.62	N180 I

^aSeveral spectra, especially the HeII lines of the early-type sources, show clear Lorentzian-shaped absorption lines, while others display Gaussian or Voigt profiles. The displayed values are obtained from applying the closest matching distribution, determined via χ -square fitting.

^b the MUSE data does not cover the NIII and NIV lines necessary to determine spectral peculiarities such as the ((f*)) or the ((f)) type.

^c In this work we adopt the O-type classification (rather than the B-type) for this source, given the detection (although weak) of the HeII line and we aim at exploring the upper limit of *Q*₀ values.

^d from Zaritsky et al. (2004).

^e obscured by HII region material.

^f As noted in Section 3.2, LH 118-105 and LH 118-182 are most likely not associated with N180, but they are included here for completeness.

^g B-type star in N180 D, included here for completeness.

Table 4: Same as Table 3 for N180.

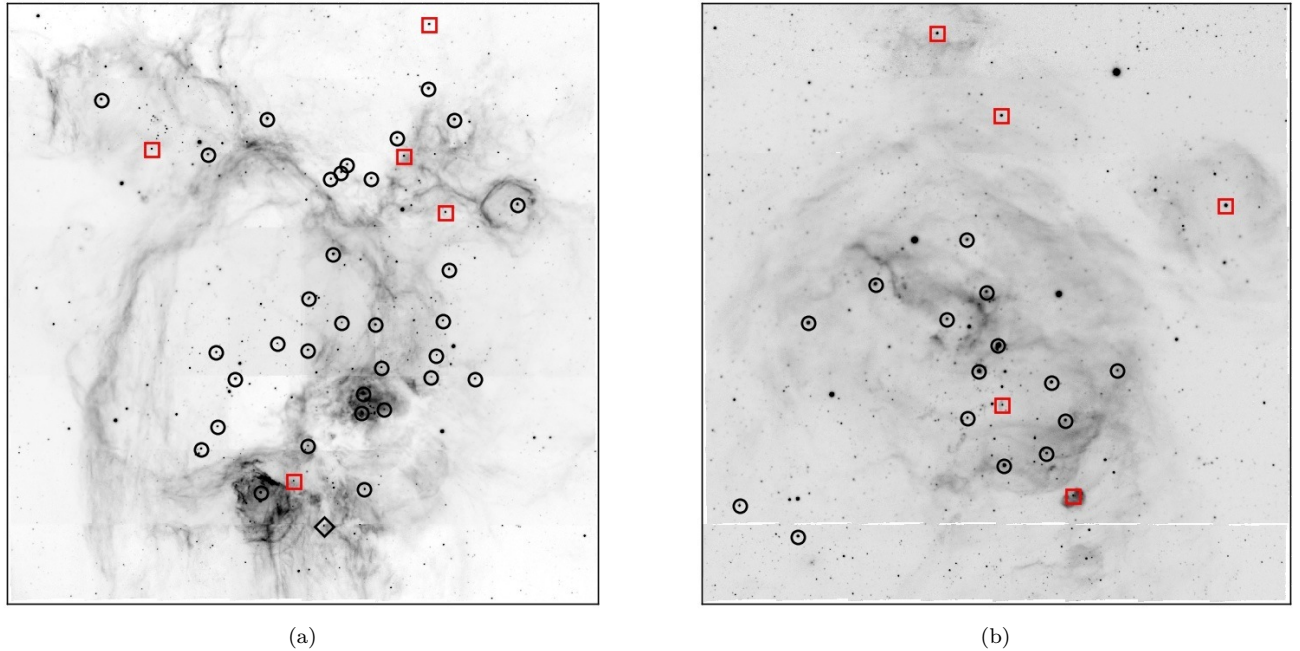


Figure 2. O-type stars in N44 (a) and N180 (b) on the [SII]6717 map. Black circles mark already known O stars, while red squares mark the objects newly identified in this work. The black diamond in N44 marks the position of the only WR star in the analysed regions.

of north) of ~ 65 pc ($4.5'$), and a minor axis of ~ 44 pc ($3'$). Except for N44 A, all other compact HII regions have formed along the western rim of N44 main. N44 A is an irregularly-shaped HII region consisting of an eastern bubble around a single O star (LH 48-9), while the majority of the LH 48 cluster stars are located further west, including LH 48-111 and MUSE N44-2. N44 B is a roughly round-shaped HII region around [WBD97] N44 6, with a radius of approximately 6.5 pc. As already noted in Nazé et al. (2002) (where this bubble is referred to as N44 F), two pillar-like structures have formed along the western rim of N44 B. These are protruding into the HII region from the surrounding cloud and are pointing back directly towards [WBD97] N44 6, which is the source most likely shaping these pillars. N44 C is about 14 pc across, it hosts 3 O-type stars and displays dusty filamentary features around its rim. N44 D is among the brightest in N44, and while it is very similar to N44 C in size ($R_{90} \simeq 7.4$ pc), it hosts a single O5 star (LH 47-338). As can be seen in Fig. 1, both N44 D and the region surrounding the WR star show bright filaments extending to the SW, and are characterised by very bright [SII] emission. Alongside the morphologically-defined HII regions just described, N44 also displays several regions of ionised gas and associated ionisation fronts, all associated with at least one identified O star. However, given that these do not have a continuous bubble/shell-like structure, we do not include them in our subsequent analyses in this paper.

N180 (DEM L326), located about 1.3° SE of 30 Doradus, consists of a gaseous, round main bubble (N180 main) with a diameter of about 78 pc ($5.4'$), into which filamentary- and pillar-like structures protrude. At the tip of one of these pillar-like structures an early-type B young stellar object (YSO) of about $12 M_\odot$ (Caulet et al. 2008) has formed, which is launching an 11 pc long bipolar jet.

This jet, HH 1177, is the first ionised jet from a high-mass YSO identified outside of our Galaxy, and it is associated with bow-shock structures above and below the pillar where it interacts with the surrounding medium (see McLeod et al. 2018 for a detailed analysis of the object). Four smaller HII regions are located around N180 main, with N180 main hosting the open cluster NGC 2122. All the smaller HII regions around N180 main contain a single O star (or, in the case of N180 D, a B-type star). With a radius of 3.4 pc, N180 C is the smallest of all the subregions. Just south of N180 A we identify a more diffuse region of ionised gas associated with the O7.5 V star MUSE N180-2.

4.2 Luminosities, electron densities and ionisation structure

H α luminosities are measured from circular apertures of radius R_{90} on the MUSE H α map and assuming a distance of 50 kpc to the LMC. We measure the total H α luminosity of the two mosaics to be $L(\text{H}\alpha)_{\text{N44}} \simeq 38.25 \text{ erg s}^{-1}$ and $L(\text{H}\alpha)_{\text{N180}} \simeq 38.06 \text{ erg s}^{-1}$. We assume a 10% measurement error on the H α flux from aperture photometry (see Appendix). In the case of N44 the value derived here is about 1.8 times lower than reported in Lopez et al. (2014) (L14 henceforth), however the region considered by these authors is larger and also encompasses the nebulosity associated with LH 49 about 6 arcminutes south of N44 main (see Fig. 1 in Nazé et al. 2002).

With the assumption of Case B recombination ($T = 10^4$ K), $Q(\text{H}\alpha)_{\text{caseB}} = 7.31 \times 10^{11} L(\text{H}\alpha) \text{ s}^{-1}$ (Osterbrock & Ferland 2006), these H α luminosities translate to a number of (log) Lyman continuum photons of 50.10 s^{-1} and 49.91 s^{-1} for N44 and N180, respectively. Luminosities and the computed $Q(\text{H}\alpha)_{\text{caseB}}$ values for the *individual* regions

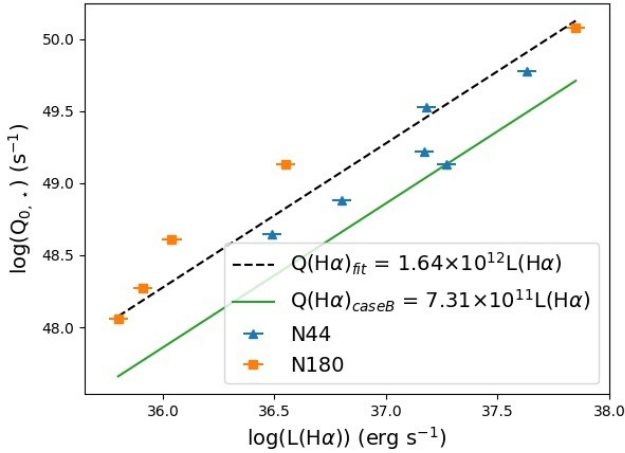


Figure 3. Measured $H\alpha$ luminosity vs the ionising photon flux $Q_{0,*}$ as derived from the spectral types of the stellar population in each region (see Table 7). The dashed black line indicates the best fit to the data, while the solid green line corresponds to the luminosity-photon flux relation as obtained from Case B recombination (Osterbrock & Ferland 2006, see section 4.2). Errors on the measured luminosity are assumed to be $\pm 10\%$ (see Appendix).

are listed in Table 7. We discuss the implications of the difference between the photon flux as derived from the spectral types of the stars in each region and that derived from the $H\alpha$ luminosity in Section 6. Here, we test the analytical relation between $L(H\alpha)$ and $Q(H\alpha)_{\text{caseB}}$ by comparing the measured $H\alpha$ luminosity to the photon flux for each region as derived from the stellar content⁵ ($Q_{0,*}$). This is shown in Fig. 3, where $Q_{0,*}$ is plotted against $L(H\alpha)$. The linear fit to the data points translates to a relation where

$$QH\alpha_{\text{fit}} = 1.64 \times 10^{12} LH\alpha \quad s^{-1} \quad (1)$$

When compared to the Osterbrock & Ferland (2006) Case B relation (hence for an optically thick nebula) between the measured luminosity and the photon flux, Eq. 1 suggests that the production of an observed $H\alpha$ luminosity via the photon flux injected by a stellar population is less efficient. Hence, an interpretation of this could be that the ratio of Eq. 1 and Case B corresponds to the fraction of photons that escape the nebula and do therefore not contribute to the luminosity. However, the difference between the Case B relation and the one found here ($Q(H\alpha)_{\text{fit}}$) is only about a factor 2, which could be explained with the assumed temperature of 10^4 K: for a temperature of 7000 K, the difference between Case B and Eq. 1 is reduced to

⁵ In this paper the used notation is as follows:

- $Q(H\alpha)_{\text{caseB}}$ refers to the number of LyC photons as derived according to Osterbrock & Ferland (2006) for Case B recombination;
- $Q_{0,*}$ refers to the number of ionising photons as measured from the derived spectral types of the analysed stellar population;
- $Q(H\alpha)_{\text{fit}}$ corresponds to the number of LyC photons as obtained by comparing the measured $L(H\alpha)$ to the ionising photon flux as obtained from the stellar population, $Q_{0,*}$;

a factor 1.7 (McKee & Williams 1997) and the conversion of ionising photon flux to $H\alpha$ luminosity is more efficient. Unfortunately, our observations are not deep enough to confidently detect the auroral $[NII]\lambda 5755$ line needed to probe temperature via the $[NII]$ emission line ratio. However, based on an electron temperatures of $> 10^4$ K derived for N44 in Toribio San Cipriano et al. (2017), we suggest that temperature is not the key player in explaining the discrepancy. To further strengthen this point we note that another factor which needs to be taken into account when considering HII region temperatures is metallicity. At lower metallicities line cooling is less efficient, and gas temperatures are therefore higher. Conversely, the translation from spectral type to $Q_{0,*}$ applied here is based on calibrations which assume solar metallicity, which introduces a further uncertainty. We will test the dependence on metallicity with MUSE observations of HII regions in the Small Magellanic Cloud (SMC), and, together with future deeper observations of more LMC (and SMC) HII regions, we will also be able to efficiently probe the electron temperature.

We compute the electron density n_e (used later in this paper to determine the pressure of the ionised gas, see 5.2) from the line ratio of the two continuum-subtracted and reddening-corrected sulphur line maps at $[SII]\lambda 6717$ and $[SII]\lambda 6731$ as in McLeod et al. 2015, assuming a temperature of 10^4 K (which is a good assumption for HII regions, Peimbert et al. 2017), and discarding pixel values with $[SII]\lambda 6717 / [SII]\lambda 6731 > 1.49$, as these lead to unphysical negative values (see Eq. 4b in McCall 1984). The resulting maps (smoothed with a Gaussian kernel) are shown in Fig. 4. Despite the mosaic pattern in N44, the morphology of the HII regions is recognisable in the density maps. Together with the RGB composites shown in Fig. 1, this illustrates the lower matter density of the main bubble of N44, the emission from the ionised gas coming from its rim, while the smaller surrounding regions are richer in gas. N180 on the other hand still shows a significant amount of ionised material in the main bubble.

The two regions show moderate electron densities, with mean values (across the entire mosaics) of $\sim 170 \text{ cm}^{-3}$ and $\sim 250 \text{ cm}^{-3}$ for N44 and N180, respectively. The values reported here are a factor 2-3 higher than the values reported in L14. These authors compute the electron density from the flux density of the free-free emission at 3.5 cm, such that n_e is proportional to the flux, the square root of the temperature, and inversely proportional to the volume of the emitting region. As noted in Peimbert et al. (2017), densities derived from radio emission are generally smaller than those obtained from the ratio of collisionally excited lines (as in this work), and the two are related via the filling factor, i.e. the fraction of a nebula filled with high-density material. Electron densities derived via these two methods are not directly comparable, and we therefore compare the values obtained via the emission line ratio method used here to similar available results from the literature. We note that the apertures used to derive mean electron densities for each region do not contain stellar residuals coming from the continuum subtraction procedure. For N44 we compare the derived mean electron density with that found in Toribio San Cipriano et al. (2017), who use VLT-UVES spectra of various LMC (and SMC) HII regions to derive abundances and physical parameters. These authors find $n_e = 200 \pm 150 \text{ cm}^{-3}$

from the [SII] line ratio for an extraction of 3.0×9.4 arcsec² centred on 05:22:13.6 -67:58:34.2 J2000 (corresponding to N44C, see Fig. 8). For the same extraction, MUSE yields $n_e = 192 \pm 36$ cm⁻³, thus in excellent agreement with the UVES results.

We investigate the ionisation structure of the two HII regions with the ratio O₂₃ ($=[\text{OII}]\lambda 7320,7330/[\text{OIII}]\lambda 4959,5007$), which traces the degree of ionisation. This is shown in Fig. 5. In N44, the highest degree of ionisation (lowest O₂₃ values) correspond to the subregion N44 D (N44 A, B and C clearly being traced by higher degrees of ionisation as well), while the low-density cavity of N44 main shows a significantly lower degree of ionisation. The opposite is the case for N180, where the main cavity shows the lowest O₂₃ values, together with N180 D.

Overall, N180 shows higher O₂₃ values, i.e. a lower degree of ionisation, than N44. With the two regions having similar densities, we suggest that the reason for this is in fact the higher number of ionising sources present in N44 (in combination with their spectral type), with the exception of the evacuated inner parts of N44 main.

4.3 Gas-phase metallicities

The so-called *strong-line method* (Alloin et al. 1979, Pagel et al. 1979) to determine chemical abundances in Galactic and extragalactic HII regions is a widely accepted and used procedure. The method relies on the measurement of emission line ratios, which are then converted into metallicity according to empirically-derived relations that link the line ratios and the metallicity and which are based on oxygen abundances computed via the *direct Te-method* (e.g. Lin et al. 2017, Pérez-Montero 2017, Pilyugin & Grebel 2016, McLeod et al. 2016a, Westmoquette et al. 2013, Monreal-Ibero et al. 2012, Bresolin et al. 2012). Despite the uncertainties introduced by the empirical relations, this method of deriving gas-phase metallicities is preferred over theoretical calibrations, as these do generally not reproduce observed oxygen abundances (Pilyugin et al. 2012).

As MUSE covers all the necessary emission lines to derive the electron temperature T_e (e.g. [NII] $\lambda 5755$, [NII] $\lambda 6548$, [NII] $\lambda 6584$), it would be possible to derive oxygen abundances via the T_e -method from this data set. However, given the short exposure time used for this program and due to the [NII] $\lambda 5755$ auroral line being very faint and hence indistinguishable from the continuum on a single pixel basis (as already mentioned above), a resolved map of this line would be completely dominated by noise. To determine gas-phase metallicities we therefore use the abundance indicators O₃N₂ and N₂ (e.g. Monreal-Ibero et al. 2011) and compute oxygen abundances according to the empirical relations given in Eq. 2 and 4 in Marino et al. (2013). The line ratios used are defined as⁶

$$\text{O3N2} = \log\left(\frac{\text{OIII}5007}{\text{H}\beta} \times \frac{\text{H}\alpha}{\text{NII}6583}\right) \quad (2)$$

⁶ For brevity we omit the wavelength symbol λ henceforth when referring to emission lines.

$$\text{N2} = \log\left(\frac{\text{NII}6583}{\text{H}\alpha}\right) \quad (3)$$

Figures 6 and 7 show the maps of the line ratios given in Eq. 2 and 3 (upper panels), as well as the derived oxygen abundances (lower panels). As discussed in e.g. Ercolano et al. (2012), deriving abundances of spatially resolved regions from integral field spectrographs introduces a series of caveats. Non-trivial dependencies of the derived values on the density and temperature trace the ionisation structure of the observed nebula, and lead to falsely low abundances for regions with a higher degree of ionisation (McLeod et al. 2016a). This can be readily seen when comparing the degree of ionisation traced by O₂₃ (Fig. 5) and the derived oxygen abundances (lower panels in Figures 6 and 7): low O₂₃ values (high degree of ionisation), found in N180 main and the smaller HII regions, show much lower O/H values than the denser gas that forms the shells. The N₂ ratio shows low values at higher degrees of ionisation (given the Balmer line in the denominator), while O₃N₂ shows a positive relation with O₂₃, due to the dominating [OIII] emission.

We compare the obtained O/H values to those derived via the classical T_e -method in Toribio San Cipriano et al. (2017) (henceforth referred to as TSC17). These authors derived ionic and total abundances for LMC and SMC HII regions from VLT-UVES spectroscopic data. Their sample does not include N180, meaning that the following discussion is based on the comparison of values obtained for N44 only. For this region, TSC17 extract a spectrum from a 3.0×9.4 arcsec region centred on 05:22.13.6 -67:58:34.2 (J2000), which is within the small HII region N44 C. A zoomed-in version of the O₂₃ map (Fig. 8) shows that the extraction region lies within the N44 C HII region (and does not contain stellar residuals resulting from the continuum subtraction, see Section 2), therefore displaying a high degree of ionisation. Table 6 compares the O/H values as obtained via the strong-line method in this work and the T_e -method of TSC17. It is clear that the high degree of ionisation in N44 D leads to much lower O/H values when compared to the T_e -derived values, and when compared to the mean of all data points.

The mean value obtained from all data points reported in Table 6 agree very well, within errors, with the value from collisionally-excited lines of TSC17. To check for consistency we perform a cut based on a threshold corresponding to the 90% contour shown in Fig. 9. After the cut we find mean O/H values (from N₂ and O₃N₂, respectively) of 8.30 ± 0.06 and 8.33 ± 0.09 for N44; 8.27 ± 0.10 and 8.28 ± 0.09 for N180 (stellar residuals, as mentioned in Section 2, are masked before deriving mean abundances). For N44, the best agreement with TSC17 is found between the O/H values derived from the collisionally-excited line (CEL) method and the N₂ ratio, although the difference between the values obtained from O₃N₂ and N₂ is minimal. The discrepancy between the values obtained in this work and those obtained in TSC17 from recombination lines (RLs) remains large. From a sample of 5 HII regions in the LMC and 4 in the SMC these authors find a better agreement between stellar abundances and those derived from CELs (rather than those derived from RLs) for low-metallicity environments such as the LMC. We therefore take the mean of the oxygen abundances derived from the N₂ and O₃N₂ lines to be a reliable value,

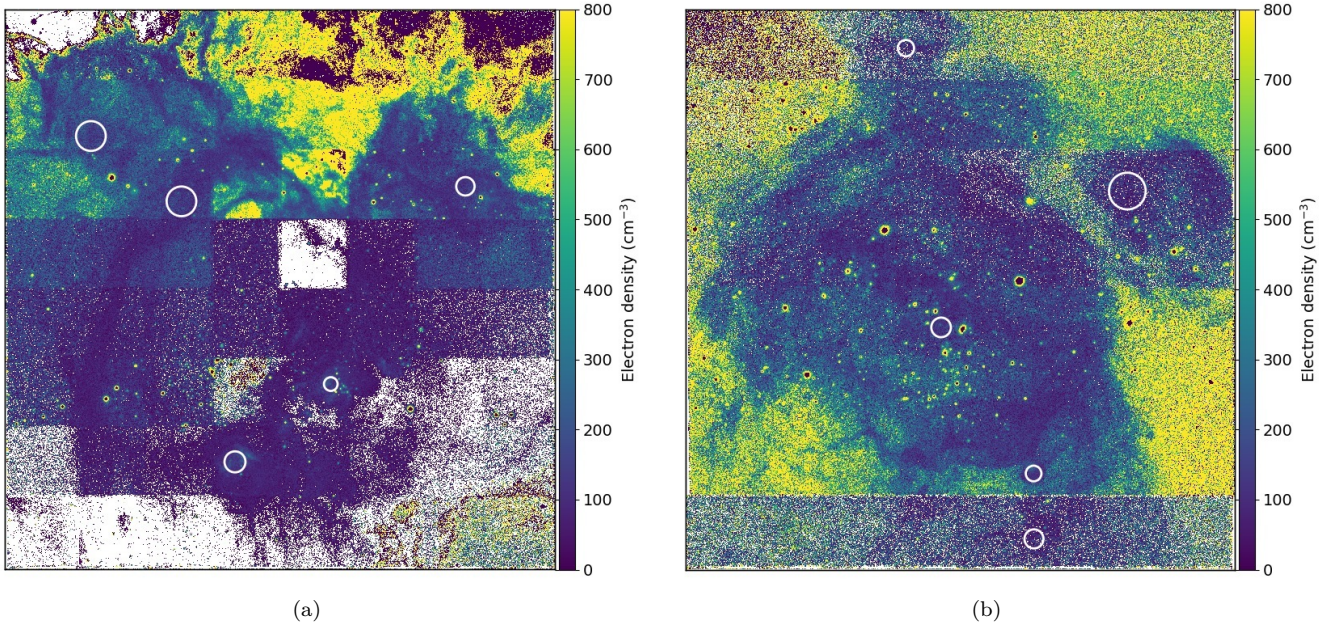


Figure 4. Electron density (n_e) maps of N44 (left) and N180 (right). White circles show the apertures used to extract n_e values reported in Table 5. Over-subtraction of the continuum in the $H\beta$ map, used in the dereddening procedure of the emission line maps, leads to residuals at the location of stellar sources (see text Section 2.)

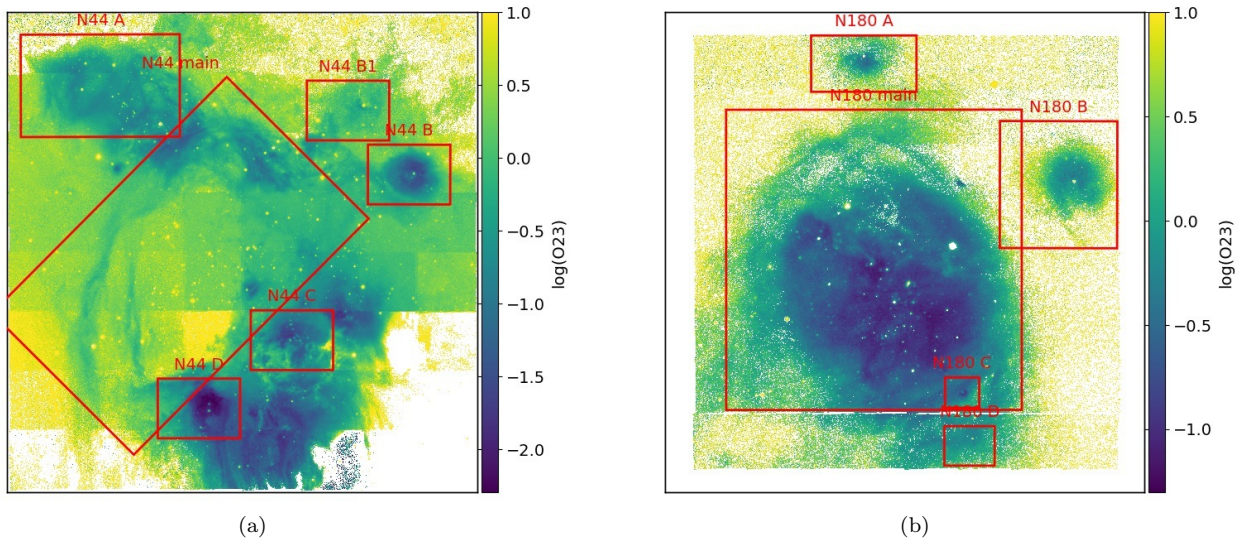


Figure 5. The emission line ratio $O23$ ($=[\text{OII}]\lambda_{7320,7330}/[\text{OIII}]\lambda_{4959,5007}$), tracing the degree of ionisation, of N44 (left) and N180 (right). Individual subregions are marked in red to facilitate the discussion in Section 4.2. Stellar residuals can be seen where the continuum subtraction of the [OII] maps is not optimal, due to the selected continuum for these lines being ~ 100 Å away from the emission lines (see Table 1).

which corresponds to 8.32 ± 0.08 for N44 and 8.28 ± 0.10 for N180. These agree very well with Russell & Dopita (1992), who find $O/H + 12 = 8.35 \pm 0.06$ as derived from HII regions in the LMC, and is consistent with an almost flat radial O/H gradient (TSC17). However, further investigation is needed to better understand the dependence of the oxygen abundance not only on the degree of ionisation in spatially-resolved nebulae, but also on metallicity.

We note that the Marino et al. (2013) calibrations used

here to derive the oxygen abundance were chosen because they are among the calibrations with the most complete HII region observations in terms of metallicities and quality. Other widely used calibrations for $N2$ and $O3N2$ are e.g. those of Pettini & Pagel (2004). However, as discussed in Marino et al. (2013), the difference between their and the Pettini & Pagel (2004) calibrations is mainly caused by the Pettini & Pagel (2004) study lacking high-quality auroral line observations. We have tested the difference between the

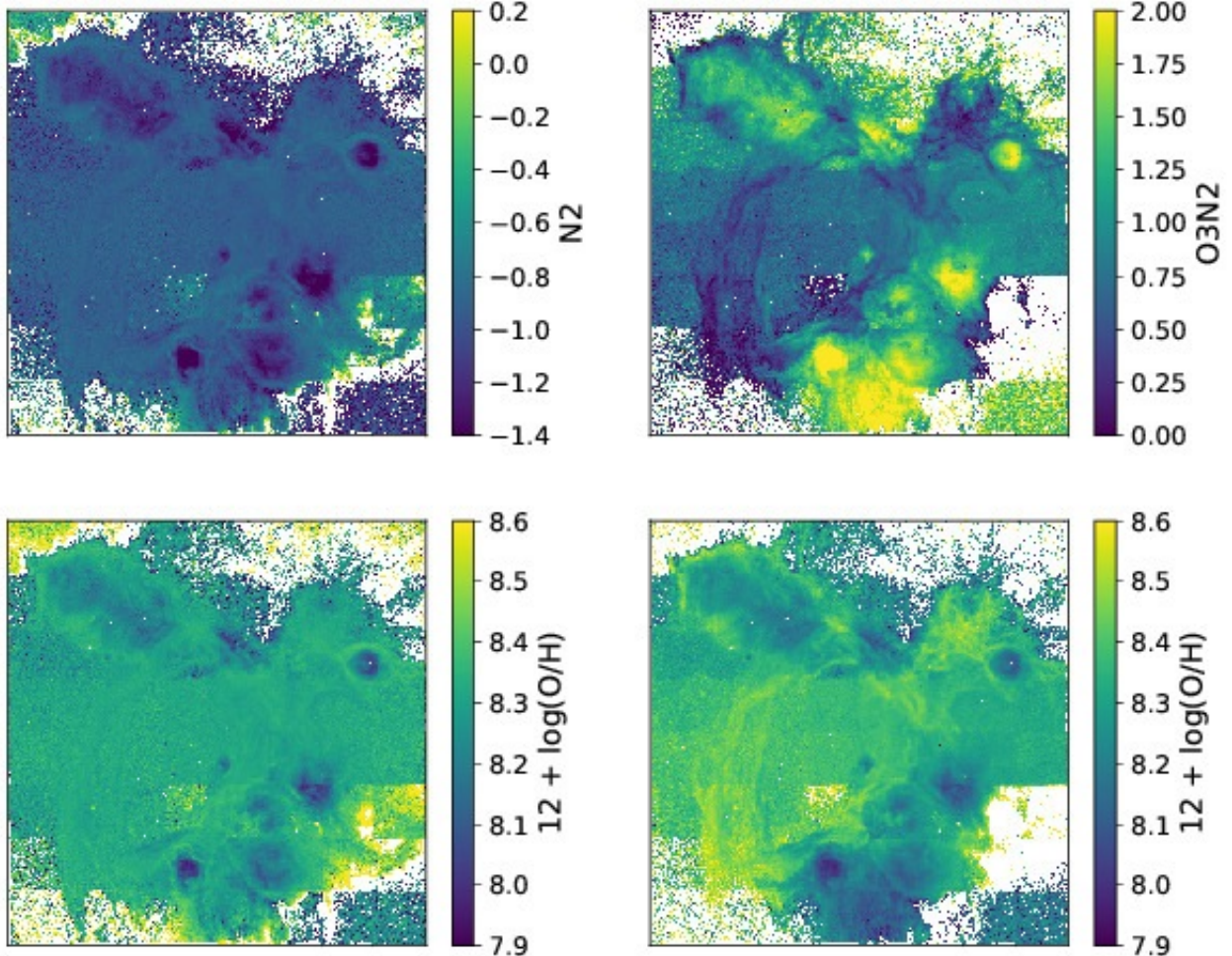


Figure 6. The N_2 and O_3N_2 line ratio maps (upper left and upper right, respectively) and the derived oxygen abundances of N_{44} . Over-subtraction of the continuum in the $H\beta$ map, used in the dereddening procedure of the emission line maps, leads to residuals at the location of stellar sources (see text Section 2.)

two by replicating the oxygen abundance analysis performed here with the Pettini & Pagel (2004) calibrations (not shown here). We find that the steeper O_3N_2 -O/H relation of Pettini & Pagel (2004) leads to even lower O/H values for high O_3N_2 regions, i.e. regions with a high degree of ionisation. By using the Marino et al. (2013) we still find values lower than the O_3N_2 fit interval (dashed horizontal lines in Fig. 9), however these only contribute to $\sim 5\%$ to the data points in the 90% contour level (used to determine mean oxygen abundances). Other emission line ratios can be used to derive oxygen metallicities, an excellent example being the R_{23} parameter which does not show a dependence on the ionisation parameter as the ratios used here (Relaño et al. 2010). However, MUSE does not cover the necessary [OII] lines (\sim

3727 \AA) needed in order to confidently use the associated empirical relations to obtain oxygen abundances.

4.4 Kinematics

We compute radial velocity maps by fitting emission lines on a pixel-by-pixel basis. For this we proceed as in MC15, where it is shown that stacking a number of different emission lines leads to a better sampling of MUSE spectra. Here, we stack $H\alpha$, [NII]6548,84 and [SII]6717,31, lines originating from the ionised gas. The underlying assumption is that the emission lines used in the stacking procedure are coming from the same line-emitting region. It is therefore a useful procedure to determine radial velocities averaged over entire regions,

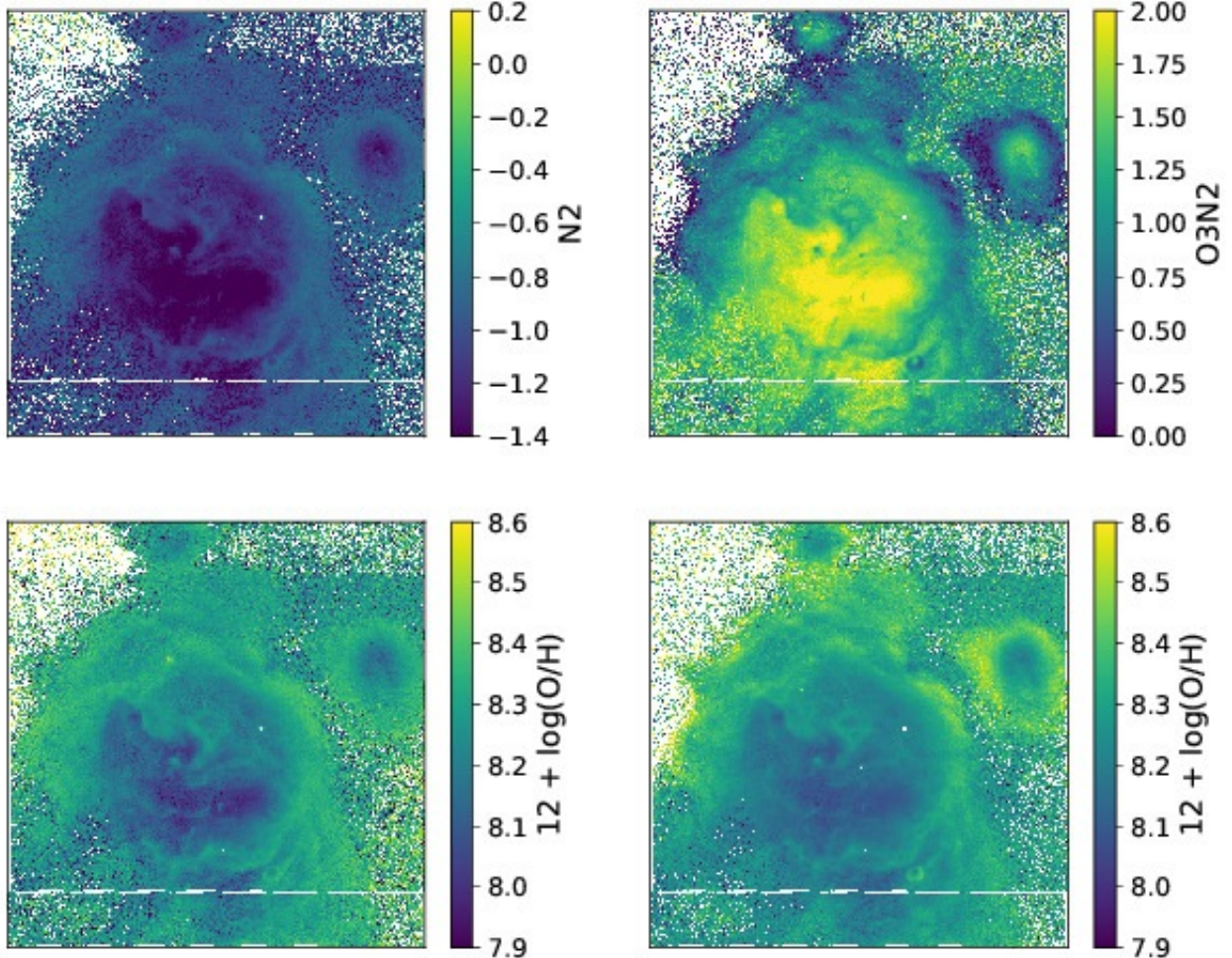


Figure 7. The N2 and O3N2 line ratio maps (upper left and upper right, respectively) and the derived oxygen abundances of N180. Over-subtraction of the continuum in the H β map, used in the dereddening procedure of the emission line maps, leads to residuals at the location of stellar sources (see text Section 2.)

but in the case of observations of entire spatially resolved HII regions the coverage of a large range of spatial scales with complicated morphologies and sub-structuring, the assumption is no longer valid. Hence, expansion velocities of the individual subregions are derived from the differential velocities across the [SII]6717 velocity maps (shown in Fig. 10). Given that the [SII] emission is typically more localised than the diffuse H α emission (Weilbacher et al. 2015), the expanding shells are best traced in [SII].

The shells in N44 are filamentary and sub-structured, and clearly recognisable as expanding ring-like structures. Expansion velocities range from ~ 6 to ~ 11 km s $^{-1}$, in good agreement with literature values (e.g. Nazé et al. 2002). The ionised gas in N180 is mainly moving towards the ob-

server, and mean shell velocities are higher than those found for N44. This is supported by Nazé et al. (2001) who find blueshifted expanding shells within N180 main with velocities of 10-20 km s $^{-1}$.

The systemic velocities of the two regions (~ 294 and 245 km s $^{-1}$ for N44 and N180, respectively) as derived from the ionised gas agree with the global dynamics of the LMC. We demonstrate this by locating the central coordinates of N44 and N180 on the radial velocity map for the LMC as traced by Gaia, as is shown in Fig. 12. For this, we cross-match the Catalog of Stellar Spectra (Skiff 2014) with the recent Gaia DR2 (Gaia Collaboration et al. 2018), and select all sources within 10° of the LMC. We then separate the sources most likely belonging to the LMC (rather than

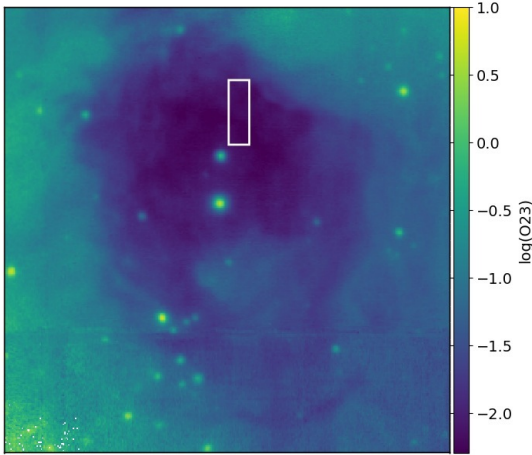


Figure 8. O₂₃ map of N₄₄ D, showing the region analysed in [Toribio San Cipriano et al. \(2017\)](#) (see text Section 4.3). Stellar residuals can be seen where the continuum subtraction of the [OII] maps is not optimal, due to the selected continuum for these lines being ~ 100 Å away from the emission lines (see Table 1).

Bubble	Central Coordinates (J2000)	R ₉₀ (pc)	n_e (cm ⁻³)	v (km s ⁻¹)
N44 main	5:22:17.2 -67:56:32.8	45.7	133±43	11.5±6.6
N44 A	5:22:30.6 -67:53:29.5	17.2	163±50	10.2±6.1
N44 B	5:21:38.3 -67:54:52.2	6.5	129±31	11.1±5.8
N44 B1	5:21:46.4 -67:53:40.9	9.1	132±32	8.4±6.6
N44 C	5:21:58.1 -67:57:28.7	7.2	152±42	6.1±5.4
N44 D	5:22:13.7 -67:58:46.8	7.4	143±42	9.3±6.2
N180 main	5:48:55.2 -70:03:33.5	39	127±44	16.9±6.7
N180 A	5:49:00.1 -69:59:47.4	6.6	122±75	15.3±4.7
N180 B	5:48:14.7 -70:02:05.1	12.2	105±61	18.2±7.3
N180 C	5:48:37.7 -70:06:02.3	3.4	137±47	12.3±13.7
N180 D	5:48:36.5 -70:06:56.0	4.6	97±62	16.4±11.7

Table 5: Central coordinates (column 2), radius containing 90% of the H α emission (column 3), electron density (column 4) and expansion velocity of the observed subregions. See text Section 4.

being foreground sources) by further selecting sources with radial velocities within the range 190–387 km s⁻¹ (as determined from HI emission in [Kim et al. 1998](#)), and plot these weighted by their radial velocity values. The rotation of the LMC disk is clearly recovered with the Gaia data, as can be seen when comparing the lower panel of Fig. 12 with Fig. 3 in [Kim et al. \(1998\)](#).

Furthermore, we determine the radial velocities of the O-type stars from the HeII line centroid. The upper panel of Fig. 11 shows the resulting histograms of the stellar radial velocities, fitted with a Gaussian distribution (for N180, we exclude LH 118-165 and LH 118-182 from the fit, as these are most likely not associated with N180). The lower panels show that there is no obvious relation between the locations of the O-stars and their radial velocity.

5 RADIATIVE AND MECHANICAL FEEDBACK

We now analyse feedback measures related to the radiation and stellar winds emitted by the massive stars that have formed within N₄₄ and N180. These are the direct radiation pressure P_{dir} (related to the deposition of kinetic energy and momentum by stellar photon flux), the pressure P_{ion} exerted by the warm ($T \sim 10^4$ K) ionised gas, and the thermal pressure from the shock-heated winds, in a similar fashion as described in L14. These authors derive these and other feedback-related quantities in a comprehensive multi-wavelength analysis of HII regions in the LMC and SMC, ranging from the X-Rays to the infrared, using optical SHASSA data to determine P_{dir} and P_{ion} . L14 conclude that the pressure of the warm ionised gas dominates over the other pressure terms, with the direct radiation pressure being the weakest term. The radii of the HII regions in their sample range from about 30 to well over 100 pc, and L14 suggest that the role of direct radiation pressure could be better analysed with a sample of younger, smaller HII regions. Except for the two main bubbles, all subregions analysed in this work are an order of magnitude smaller in size than the L14 sample, therefore enabling an extension of the work of L14 towards smaller radii.

5.1 Direct radiation pressure

L14 compute the volume-averaged direct radiation pressure assuming a spherical HII region. Because MUSE offers a much higher angular resolution than the SHASSA survey (0.2"/pixel vs. 47.64"/pixel), we can now compute the direct radiation pressure for all subregions rather than averaging over what is clearly a population of different HII regions that vary in age, size and stellar content. For this we use Eq. 3 in [Pellegriani et al. \(2007\)](#),

$$P_{\text{dir}} = \frac{Q_{0,*} \langle h\nu \rangle}{4\pi R^2 c} \quad (4)$$

where $\langle h\nu \rangle$ is the mean photon energy (here we adopt $\langle h\nu \rangle \sim 15$ eV, [Pellegriani et al. 2007](#)) and $R = R_{90}$. This form is directly comparable to the radiation pressure force integrated at the ionisation front, where our electron densities and HII regions pressure terms are measured. This differs from the method used in L14, where the direct radiation pressure is derived via the bolometric luminosity measured for an HII region. However, this requires treating P_{dir} as an energy density and hence assuming full coupling with the gas, which might not be correct for evolved (i.e. evacuated) HII regions. This leads to P_{dir} as derived via the L14 method being about an order of magnitude higher than what is found here.

The radiation pressure thus computed for each subregion is listed in Table 7. P_{dir} is generally of the order of a few 10^{-13} dyn cm⁻², with the exception of N44 C and N44 D. In addition to the higher P_{dir} values, these two regions are an order of magnitude more luminous than the other regions of comparable sizes. We will further discuss these two regions in Section 7.

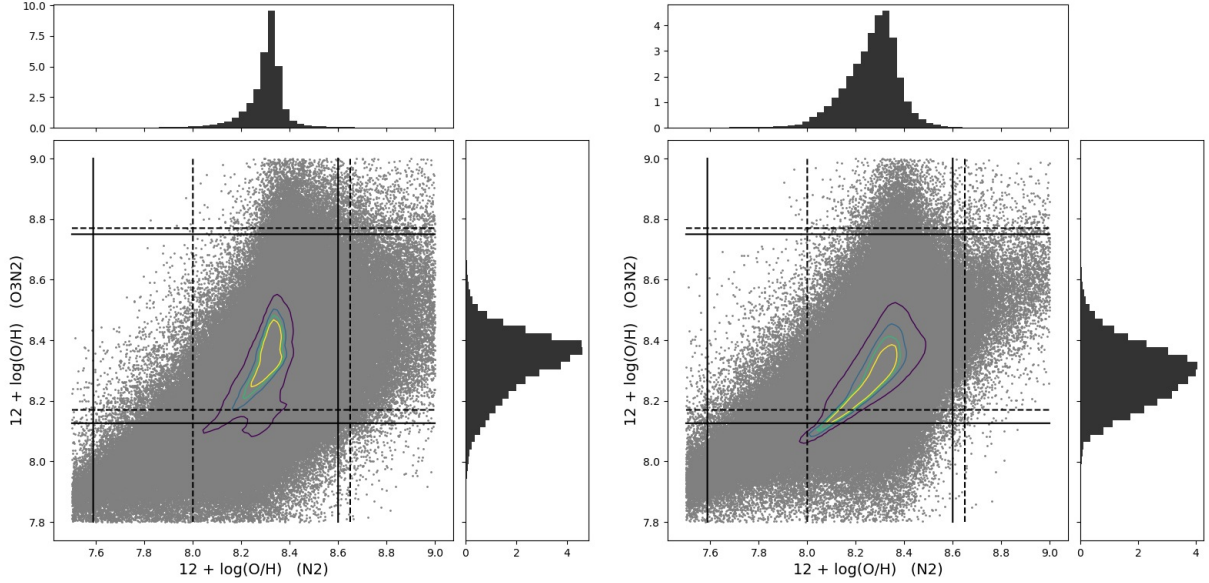


Figure 9. The oxygen abundance as derived from the N2 line ratio vs. that derived from the O3N2 ratio (left for N44 and right for N180). Contour levels (smallest to largest) correspond to 50%, 60%, 75% and 90% of data points. Shown are only data points with realistic values, i.e. for which $7.5 < 12 + \log(\text{O}/\text{H}) < 9$. Vertical and horizontal lines indicate the applicability (solid lines) and the fit (dashed lines) intervals of the Marino et al. (2013) calibrations.

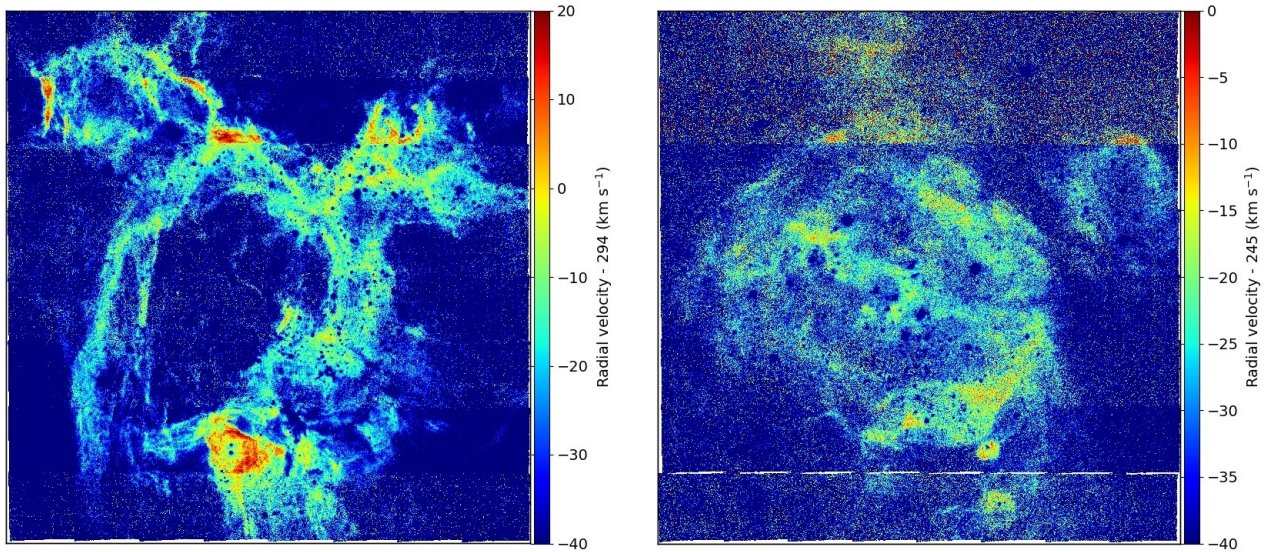


Figure 10. [SII]6717 radial velocity maps for N44 (left) and N180 (right).

5.2 Pressure of the ionised gas

Following L14, the pressure of the ionised gas is computed via

$$P_{\text{ion}} = n_e + n_{\text{H}} + n_{\text{He}}kT_e \approx 2n_e kT_e \quad (5)$$

which follows from the ideal gas law, under the assumption that helium is singly ionised. As motivated earlier, we assume an HII region temperature of 10^4 K, and estimate P_{ion} from the electron density. The pressures of the ionised

gas as computed via Eq. 5 are listed in Table 7. Because of n_e being the only free parameter in this pressure term and the subregions all having similar electron densities, the variation in P_{ion} values is limited, $\sigma(P_{\text{ion}}) \approx 0.5 \times 10^{-11}$ dyn cm^{-2} . A larger sample of HII regions in different environments is needed to further investigate the ionisation pressure. Together with T_e measurements via the temperature-sensitive [NII] line ratio from deeper MUSE observations, a large sample of observed HII regions would allow to obtain

N44 D		N44 all		Toribio San Cipriano et al.	
N2	O3N2	N2	O3N2	RLs ^a	CELS ^b
8.04±0.06	8.02±0.02	8.30±0.10	8.32±0.11	8.58±0.02	8.31±0.03

^aRecombination lines.

^bCollisionally excited lines.

Table 6: Oxygen abundance in units of $12 + \log(\text{O}/\text{H})$ as measured for N44 D (corresponding to the same region as in TSC17, see Fig. 8) and as measured for the entire mosaic, derived via the two emission line ratios N2 and O3N2, for the mean of all data points, and the T_e -derived values reported in TSC17.

a larger spectrum of P_{ion} values across a range of different environments, sizes and stellar content.

5.3 Stellar winds

At very early, compact stages, the expansion of HII regions is governed by stellar winds. With parsec-scale radii, the HII regions examined in this work do not classify as ultra-compact HII regions for which this would be the case, but given that they present ring-like morphologies and kinematics of expanding shells, and given the existence of wind-blown superbubbles (e.g. Oey & Massey 1994), the contribution from winds from O-type stars needs to be addressed. For this we compute the stellar wind luminosity given the observed bubble radii, densities and dynamical timescales, and derive the wind pressure of the hot, wind-shocked gas according to Tielens (2005):

$$R \simeq 32 \left(\frac{L_w}{10^{36} \text{ erg s}^{-1}} \right)^{15} \left(\frac{0.5 \text{ cm}^{-3}}{n_0} \right)^{15} \left(\frac{t}{10^6 \text{ yr}} \right)^{35} \text{ pc} \quad (6)$$

$$P_w \simeq 2.3 \times 10^{-12} \left(\frac{L_w}{10^{36} \text{ erg s}^{-1}} \right)^{25} \left(\frac{n_0}{0.25 \text{ cm}^{-3}} \right)^{35} \left(\frac{10^6 \text{ yr}}{t} \right)^{45} \text{ dyn cm}^{-2} \quad (7)$$

where L_w is the wind luminosity, $R = R_{90}$, $n_0 = n_e/0.7$ (McLeod et al. 2016b) and t the dynamical timescale.

We compare the wind luminosities as computed by rearranging Eq. 6 to wind luminosities obtained by directly considering the stellar population in each region, i.e.

$$L_{w,*} = \frac{1}{2} M v_\infty^2 \quad (8)$$

where M is the stellar wind mass-loss rate and v_∞ the terminal wind velocity. For this we use mass-loss rates and terminal velocities from Table 1 in Muijres et al. (2012) (for M we use the last column, and we compute the terminal velocity as 2.6 times the escape velocity, all used values are listed in Table C1). As can be seen from Table 7, for seven subregions the wind luminosities derived via Eq. 6 (which assumes that the bubble size is entirely set by stellar winds) are higher than those predicted from the stellar population. For two subregions, N44 C and N44 D, which also show higher P_{dir} values, the opposite is the case, while for N44 A and N44 B L_w and $L_{w,*}$ are roughly comparable. We will discuss the implications of this in Section 7.

A major uncertainty in the computation of stellar winds from the spectral types of the stellar content is the metallicity used for the prediction of the mass-loss rate. Muijres et al. (2012) adopt solar metallicity, whereas M scales as $Z Z_\odot^\alpha$, with $\alpha = 0.69$ (Vink et al. 2001). As winds are line-driven, lower metallicities imply fewer lines, hence less momentum transfer, weaker winds and overall less mass-loss. The computed L_w values are therefore almost certainly overestimated and strict upper limits. Dedicated models predicting mass-loss rates and terminal velocities for half-solar metallicity are needed to better compare L_w and $L_{w,*}$ in the LMC.

Furthermore, we note that while the theoretical mass-loss rate predictions used to derive wind luminosities from the observed spectral types agree with empirically-derived mass-loss rates (e.g. de Jager et al. 1988, Mokiem et al. 2007) in the $\log(L/L_\odot) > 5.2$ regime, problems occur for O stars with lower luminosities. However, given that it remains unclear whether this problem (referred to as the *weak-wind problem*, e.g. Marcolino et al. 2009) arises from observations or theory and given the good agreement at higher luminosities, for consistency we use the theoretical predictions for the low-luminosity regime as well.

6 PHOTON LEAKAGE

Of the ionising photons emitted by massive stars, most are absorbed and therefore go into the heating budget of an HII region. However, a fraction of the photons can escape from the region into the diffuse galactic ISM, hence contributing to the overall energetics of the host galaxy. Determining said fraction of escaping photons is therefore necessary not only to determine the evolution of single HII regions, but also when discussing the impact of massive stars on galaxy evolution. Calculating the escape fraction becomes possible when combining maps of the ionised gas as traced by H α and the knowledge of the stellar content of a given HII region.

Niederhofer et al. (2016) use synthetic young clusters to test a method which relies on broadband photometry to determine spectral types of massive stars, stellar atmosphere models to subsequently derive photon fluxes, and then compares the integrated flux from a given stellar population to the same as derived from narrowband H α maps. These authors find that the high uncertainties introduced by determining spectral types from broadband photometry lead to this method not being reliable for determining the escape fraction of ionising photons. Moreover, they suggest that stellar spectra are needed to reduce the spectral type uncer-

Bubble	$L(\text{H}\alpha)$ erg s^{-1}	$Q(\text{H}\alpha)_{\text{caseB}}$ s^{-1}	$Q_{0,*}$ s^{-1}	f_{esc}	P_{dir} dyn cm^{-2}	P_{ion} dyn cm^{-2}	L_{w} erg s^{-1}	t_{dyn} Myr	P_{w} dyn cm^{-2}	$L_{\text{w},*}$ erg s^{-1}	Σ_{SFR} $10^{-6} \text{M}_{\odot} \text{yr}^{-1} \text{pc}^{-2}$
N44 main	37.63	49.48	49.78	0.49	0.002	3.67	37.62	3.9	1.92	36.69	0.16
N44 A	37.27	49.12	49.52	0.60	0.007	4.50	36.69	1.6	1.80	36.66	0.49
N44 B	36.80	48.64	48.88	0.42	0.012	3.56	35.84	0.6	1.67	35.81	1.18
N44 B1	36.49	48.34	48.65	0.51	0.004	3.64	35.79	1.1	0.98	35.38	0.29
N44 C	37.18	49.03	49.53	0.68	0.04	4.20	35.21	1.1	0.58	36.70	2.31
N44 D	37.17	49.02	49.22	0.37	0.02	3.95	35.76	0.8	1.26	36.49	2.13
N180 main	37.85	49.71	50.08	0.57	0.005	3.51	37.97	2.3	4.07	37.26	0.37
N180 A	36.04	47.90	48.61	0.80	0.006	3.37	36.41	0.4	4.31	35.47	0.20
N180 B	36.55	48.40	49.13	0.81	0.006	2.90	37.11	0.7	5.29	36.12	0.19
N180 C	35.91	47.77	48.27	0.68	0.011	3.78	35.39	0.3	1.92	35.09	0.56
N180 D	35.80	47.66	48.06	0.60	0.004	2.67	35.99	0.3	3.20	34.95	0.24

Table 7: Column 2: (log) $\text{H}\alpha$ luminosity derived from the MUSE $\text{H}\alpha$ map. Column 3: (log) number of Lyman continuum photons per second derived via Eq. 9 from the measured $\text{H}\alpha$ luminosity in column 2. Column 4: (log) number of Lyman continuum photons per second emitted by the O-type stars in each region. Column 5: escape fraction (see Eq. 10). Column 6: direct radiation pressure (see Eq. 4). Column 7: pressure of the ionised gas (see Eq. 5). Column 8: (log) stellar wind luminosity as derived via Eq. 6. Column 9: dynamical timescale obtained from the expansion velocity and radius of each region (Table 5). Column 10: wind pressure as derived via Eq. 7. Column 11: (log) wind luminosity inferred from the spectral type of the stellar content and determined via Eq. 8 using the values given in Table C1. Column 12: SFR per unit area computed from $L(\text{H}\alpha)$ via Eq. 11. All pressure terms are in units of $10^{-10} \text{dyn cm}^{-2}$.

tainties, and that such a study could be performed on data of the Magellanic Clouds.

Here, we take up on the results of Niederhofer et al. (2016) and compare $Q_{0,*}$ as obtained by spectroscopically identifying and classifying the O-type stars, to $Q(\text{H}\alpha)_{\text{caseB}}$ (Osterbrock & Ferland 2006) obtained from the measured $\text{H}\alpha$ luminosity,

$$QH\alpha_{\text{caseB}} \text{ s}^{-1} = 7.31 \times 10^{11} LH\alpha \text{ erg s}^{-1} \quad (9)$$

where $L(\text{H}\alpha)$ is the $\text{H}\alpha$ luminosity of a region as measured from narrowband $\text{H}\alpha$ maps, as described in Section 4.2. The fraction of photons escaping from the HII region is then given by

$$f_{\text{esc}} = \frac{Q_{0,*} - QH\alpha_{\text{caseB}}}{Q_{0,*}} \quad (10)$$

and the resulting values for each region are listed in Table 7. Escape fractions are > 0.2 for all regions (consistent for the late stage of HII expansion of low metallicity systems, Rahner et al. 2017), and overall N180 shows higher f_{esc} values than N44, a fact that is reflected in the distribution of data points in Fig. 3. For a statistically significant sample of HII regions in both the SMC and the LMC, Pellegrini et al. (2012) find that lower column densities lead to leakier HII regions, and that luminous ($\log(L) > 37 \text{ erg s}^{-1}$) regions are predominantly optically thin. Indeed, Pellegrini et al. (2012) classify N44 as an optically thin region, and N180 as a blister-type region, with column densities of 3.97 and $3.03 \times 10^{21} \text{ cm}^{-2}$, respectively. Hence, we suggest that the higher escape fractions found for N180 are a consequence of the lower column density of the complex.

Overall, Pellegrini et al. (2012) find an escape fraction of ~ 0.42 for the LMC. If the discrepancy between the measured and expected flux-luminosity relation discussed in Section 4.2 is indeed tracing the escape fraction, rather than being the consequence of systematic uncertainties, then the resulting $f_{\text{esc}} \sim 0.45$ is in good agreement with the global

value of Pellegrini et al. (2012). As mentioned before, the preliminary work presented in this paper will be augmented with in-hand/future MUSE observations of over a hundred HII regions in nearby galaxies and the Magellanic Clouds. These will be used to test the dependency of the escape fraction on a variety of HII region parameters such as density, metallicity, radius, etc.

7 DISCUSSION

To discuss the impact of feedback on star formation, we also estimate the star formation rate (SFR) for each subregion according to the relation given in Kennicutt (1998),

$$SFR \text{ M}_{\odot} \text{ yr}^{-1} = 7.9 \times 10^{-42} LH\alpha \text{ erg s}^{-1} \quad (11)$$

from which (together with R_{90}) we derive the SFR per unit area Σ_{SFR} , listed in Table 7. We note that the conversion from $\text{H}\alpha$ luminosity to SFR in Eq. 11 relies on an ensemble average over HII regions of different ages, as well as on population synthesis models. While this introduces caveats when applied to individual objects (as analysed here), it remains a meaningful exercise to estimate the level of star formation activity in our studied regions.

For the total $\text{H}\alpha$ luminosities mentioned in Section 4.2, we find total SFRs of ~ 1400 and $900 \text{ M}_{\odot} \text{ Myr}^{-1}$ for N44 and N180, respectively. The SFR of N44 is thus comparable to that of N11, while both regions have SFRs well below those of 30 Dor or N79 (Ochsendorf et al. 2017). Fig. 13 shows that together, the analysed feedback mechanisms have a negative effect on star formation by setting an upper limit to Σ_{SFR} as a function of increasing pressure (given by the $\text{H}\alpha$ surface brightness cap towards higher feedback pressures).

For our sample of smaller, more compact HII regions (compared to the L14 sample) we find that the pressure of the ionised gas generally dominates over the other pressure terms (Fig. 14) and that the direct radiation pressure is the weakest contribution. This is consistent with what L14 find

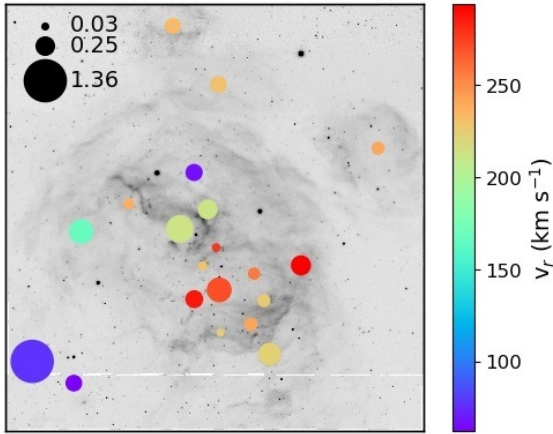
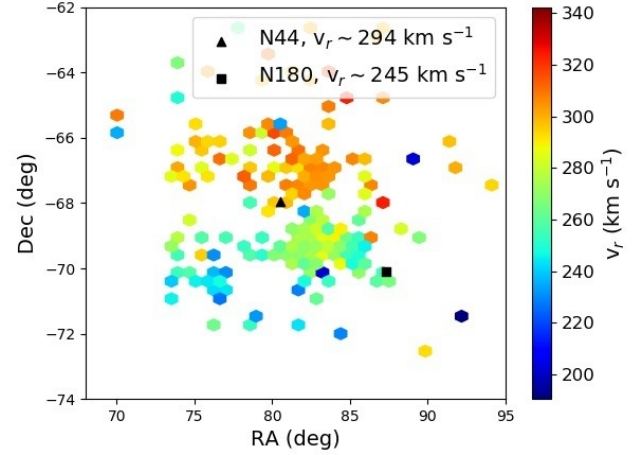
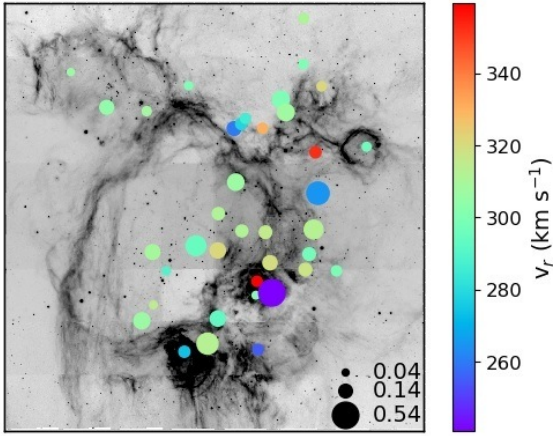
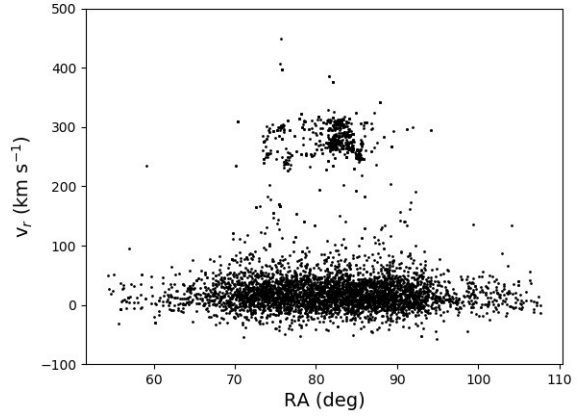
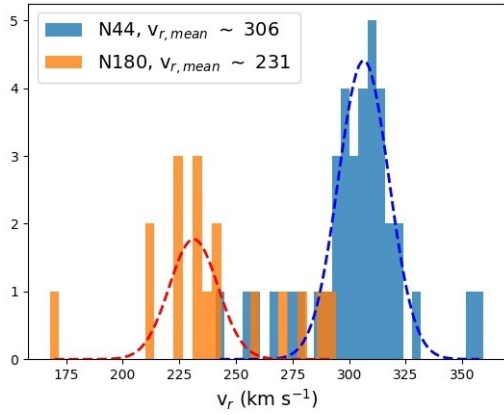


Figure 11. Upper panel: histograms of the stellar radial velocities, fitted with a Gaussian distribution. Bottom panels: O-type stars colour-coded by radial velocity for N44 and N180 (middle and bottom panels, respectively). The sizes of the circles reflect the errors on the v_r measurement. The two stars with very low radial velocities in N180 (bottom left corner of image) are not included in the histogram fit in the upper panel (see text Section 4.4).

Figure 12. Upper panel: radial velocity of stars within 10° of the LMC, selected by cross-hatching Gaia DR2 and the Catalog of Stellar Spectra (Skiff 2014). The LMC is distinguishable as the group of data points $>190 \text{ km s}^{-1}$. Lower panel: stars selected from the plot above with $190 < v_r < 387 \text{ km s}^{-1}$, the positions of N44 and N180 are indicated with a black triangle and square, respectively.

for their sample of HII region complexes. We therefore conclude that none of the HII regions are driven by radiation pressure. As already mentioned in Section 5.2, given the lack of temperature measurements and the similar sizes and electron densities of the N180 and N44 subregions, the MUSE data in this work does not allow a detailed analysis of P_{ion} as a function of HII region parameters and stellar content. However, while P_{dir} is about two-three orders of magnitude smaller than P_{ion} , P_w is only a factor of a few lower (and in some cases, e.g. N180 B, N180 main, even higher).

When considering the amount of feedback energy injected by stellar winds, we distinguish between three different regimes depending on whether the expected wind luminosity $L_{w,*}$ (as derived from the spectral types of the stars within the regions) is smaller or larger than the value obtained from a wind-driven model (L_w as per Eq. 6).

- $L_w > L_{w,*}$. For seven out of the eleven bubbles, wind luminosities as derived via Eq. 6 are too high with respect

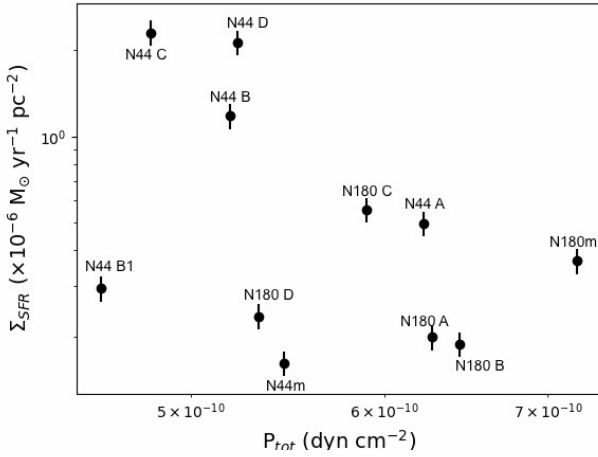


Figure 13. The star formation rate (SFR) per unit area as a function of the total pressure for each region.

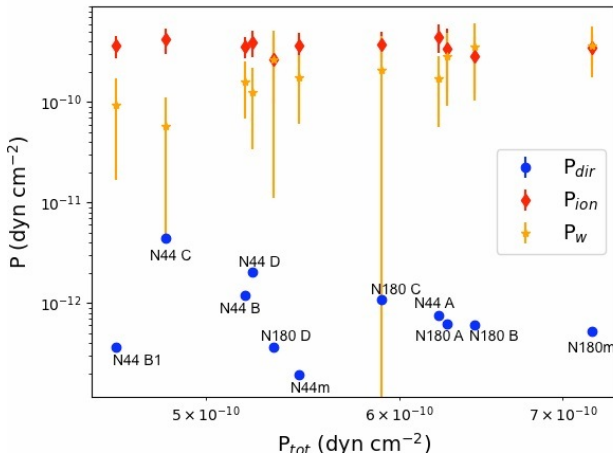


Figure 14. Individual pressure terms as a function of total pressure.

to values expected from the stellar content (i.e. derived via Eq. 8); if the measured radii are correct, then this implies that either the measured expansion velocities are too low, or that stellar winds alone are not enough to account for the measured radii. For these regions we also find the lowest contribution of the P_{dir} term to the total pressure.

- $L_{\text{w}} \sim L_{\text{w},\star}$. For two bubbles, N44 A and N44 B, the wind luminosity as derived from the stellar content ($L_{\text{w},\star}$) is roughly equal to the model value (L_{w} , derived via Eq. 6), indicating that these are consistent with the standard bubble model (Weaver et al. 1977).
- $L_{\text{w}} < L_{\text{w},\star}$. The two regions N44 C and N44 D are clear outliers in our sample. With similar sizes as the other sub-regions, N44 C and N44 D both host early-type O stars. In addition to the O5 III star LH 47-191 (the most luminous in the N44 complex, which alone drives a photon flux of $Q_{0,\star} \sim 3 \times 10^{49}$ photons s^{-1}), N44 C also harbours an O8 V and an O9.5 V star. N44 D is being illuminated by LH 47-338, an O5 V star with a photon flux of $Q_{0,\star} \sim 1.7 \times 10^{49}$

photons s^{-1} . Both show higher P_{dir} values, lower P_{w} values, and $L_{\text{w}} \ll L_{\text{w},\star}$. The latter implies a discrepancy between the mechanical energy input from the stellar population in the bubbles and their measured kinematics. In other words, if the expansion velocities are correct, then the bubbles are too small for the amount of energy available from stellar winds alone, as the injected $L_{\text{w},\star}$ alone would produce bubbles of over twice the observed size of N44 C and D over a period of ~ 1.5 Myr. Oey (1996b) refers to this as the *growth rate discrepancy*, which consists of an apparent overestimate of the wind luminosity found not only for superbubbles, but also for single-star bubbles around e.g. Wolf-Rayet stars (Oey 1996b and references therein). Assuming that the measured radii are correct, a possible solution to this would be to increase the expansion velocity by a factor $\sim 2-3$ to reconcile L_{w} and $L_{\text{w},\star}$. Another possible solution to the discrepancy would be to increase the density by about an order of magnitude. If the measured radii, expansion velocities and densities of N44 C and D are all correct, the question of why these bubbles are not larger still remains. The close proximity of N44 C and D have to the shell of N44 main could for example suggest that the expansion of the two bubbles has been slowed down by high-density material in the direction of N44 main. Indeed CO emission is detected towards N44 C and D, confirming the presence of high-density material associated with these two regions (Wong et al. 2011). As a consequence of the slower expansion we observe (relatively) higher luminosities, direct radiation pressures and star formation rates for these two regions. This suggests that for small (< 10 pc) HII regions whose expansion is at least partially confined by a high-density environment, a higher photon flux coming from the presence of early-type massive stars (which inject a significant photon flux) leads to an increased contribution of the direct radiation pressure and a decreased contribution of winds towards the total pressure (see Fig. 15).

The three regimes are displayed in Fig. 15, which shows that for $L_{\text{w}}/L_{\text{w},\star} > 1$, both Σ_{SFR} and the contribution of P_{dir} to the total pressure are low, while the opposite is the case for the *growth rate discrepancy* bubbles ($L_{\text{w}}/L_{\text{w},\star} < 1$). The three regimes therefore allow a qualitative discussion on the contribution of winds vs. other expansion-driving mechanisms. Indeed, while bubbles for which $L_{\text{w}} \sim L_{\text{w},\star}$ are consistent with being wind-driven, bubbles where $L_{\text{w}} > L_{\text{w},\star}$ require additional driving mechanisms other than only winds to account for their measured sizes the latter being also discussed in Relaño & Beckman 2005 for high-luminosity, extragalactic HII regions). In the case of the two growth-rate discrepancy bubbles, we suggest that the wind-driven expansion is slowed down due to surrounding higher-density material.

Here we have neglected the contribution of dust-processed radiation pressure, which L14 find to be comparable to the pressure of the warm ionised gas, and which could play a significant role in these two regions (particularly N44 C, which seems to be partially obscured by dusty features along its rim). With the MUSE data we cannot probe the dust-processed radiation pressure, and higher-resolution

⁷ Increasing the expansion velocity would lead to shorter dynamical timescales and therefore to higher L_{w} values.

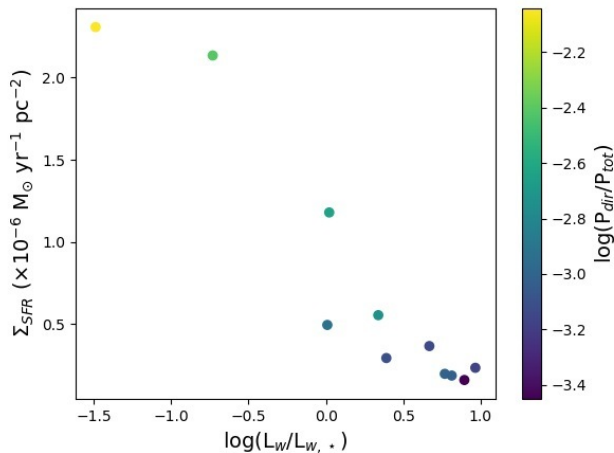


Figure 15. The star formation rate per unit areas as a function of the ratio of measured and expected wind luminosity, colour-coded by relative contribution of the direct radiation pressure ($P_{\text{dir}}/P_{\text{tot}}$).

IR observations could help disentangle the various pressure terms at these spatial scales. This could for example be achieved with complementary JWTS/MIRI observations in the 5–28 μm range.

8 SUMMARY

With data of the LMC regions N44 and N180 from the integral field spectrograph MUSE we simultaneously (identify and) classify the massive, feedback-driving O-type stars and derive the characteristics and kinematics of the feedback-driven bubbles in which the stars have formed. We analyse a total of 11 individual HII regions (with radii from 3 up to over 45 pc), which enables us to directly link the massive stellar population and feedback-related quantities of the regions. Our O star identification and classification algorithm correctly recovers all previously known O stars, and the MUSE data allows the identification of a total of 10 previously unidentified O-type stars.

When comparing the observed luminosities with those expected from the stellar content of the individual regions, we find a deviation from the typically-used conversion between luminosity and ionising photon flux of a factor of 2. Whether this is due to the stellar model parameters used to infer the ionising photon flux from a given spectral type, or whether this is inherent to the low-metallicity environment of the LMC will be tested with future observations.

We compute emission line ratio maps of the two HII region complexes and find a good agreement between derived electron density values and the literature. We investigate the ionisation structure with the O23 ratio and find that the highest degrees of ionisation are found in N44 D and N180 main. N44 main, the largest of the observed bubbles, hosting the oldest stellar population, is seemingly devoid of gas, which is reflected by a very low degree of ionisation. Furthermore, we compute oxygen abundances via the so-called strong line method and discuss the caveats of using this method for spatially resolved integral field data.

We show the dependency of the derived values on the degree of ionisation, and conclude that integrated values agree (within errors) with the direct T_e -method. Radial velocities obtained from a Gaussian fitting routine agree well with the global dynamics of the LMC disk, as demonstrated when considering radial velocities as derived from Gaia on galactic scales.

Feedback from the massive stellar population in the individual subregions is analysed by comparing the contribution of the direct radiation pressure, the pressure of the warm ionised gas and the pressure from stellar winds to the expansion of the HII regions. Overall, we find that the warm ionised gas and winds drive the expansion of the HII regions, with the ionised gas being the apparent dominant term. However, follow-up IR observations are needed to probe the contribution of dust-processed radiation pressure. Furthermore, we find that the computed photon escape fractions agree well with what is expected from literature. We also find that for the case of early-type O stars found in small (< 10 pc) regions, where the high ionising flux produces high luminosities, radiation pressure is enhanced and higher star formation rates per unit area are measured. It would be important to compare this result for lower density bubbles with a comparable stellar content (i.e. photon flux budget) to derive the characteristic properties for which the various pressure terms dominate.

We conclude that this work, together with a preliminary study of ionisation-induced photoevaporation of pillar-like structures in massive star-forming regions, demonstrates that integral field spectroscopy is a very powerful tool in the field of feedback from massive stars. However, disentangling the various feedback mechanisms only becomes possible with observations spanning a significant range of environments, as this allows to probe dependencies on metallicity, size, stellar and dust contents. We are currently planning a MUSE program targeting a statistically representative sample of HII regions in the LMC and SMC which, together with the preliminary data set presented here and in-hand MUSE data of HII regions in other nearby star-forming galaxies (e.g. McLeod et al., in prep.), will enable a robust analysis of feedback from massive stars.

ACKNOWLEDGEMENTS

This research is supported by a Marsden Grant from the Royal Society of New Zealand (AFM). JMDK gratefully acknowledges funding from the German Research Foundation (DFG) in the form of an Emmy Noether Research Group (grant number KR4801/1-1) and from the European Research Council (ERC) under the European Union’s Horizon 2020 research and innovation programme via the ERC Starting Grant MUSTANG (grant agreement number 714907). We thank M. Krumholz, P. Crowther and S. Glover for the useful discussions. This research made use of Astropy, a community-developed core Python package for Astronomy (Astropy Collaboration, 2018), as well as Astrodendro, a Python package to compute dendrograms of Astronomical data (<http://www.dendrograms.org/>), Pyspeckit (Ginsburg & Mirocha 2011), and Spectral Cube (<https://spectral-cube.readthedocs.io/>).

REFERENCES

- Alloin D., Collin-Souffrin S., Joly M., Vigroux L., 1979, *Astronomy & Astrophysics*, 78, 200
- Bacon R., et al., 2010, in *Society of Photo-Optical Instrumentation Engineers (SPIE) Conference Series Vol. 7735 of Society of Photo-Optical Instrumentation Engineers (SPIE) Conference Series*, The MUSE second-generation VLT instrument. p. 8
- Bica E., Claria J. J., Dottori H., Santos Jr. J. F. C., Piatti A. E., 1996, *The Astrophysical Journal Supplement*, 102, 57
- Bresolin F., Kennicutt R. C., Ryan-Weber E., 2012, *The Astrophysical Journal*, 750, 122
- Castro N., Crowther P. A., Evans C. J., Mackey J., Castro-Rodríguez N., Vink J. S., Melnick J., Selman F., 2018, *Astronomy & Astrophysics*, 614, A147
- Cautel A., Gruendl R. A., Chu Y.-H., 2008, *The Astrophysical Journal*, 678, 200
- Conti P. S., Garmany C. D., Massey P., 1986, *The Astronomical Journal*, 92, 48
- Crowther P. A., 2007, *Annual Review of Astronomy and Astrophysics*, 45, 177
- Crowther P. A., Dessart L., 1998, *Monthly Notices of the Royal Astronomical Society*, 296, 622
- de Jager C., Nieuwenhuijzen H., van der Hucht K. A., 1988, *A&AS*, 72, 259
- Ercolano B., Dale J. E., Gritschneider M., Westmoquette M., 2012, *Monthly Notices of the Royal Astronomical Society*, 420, 141
- Gaia Collaboration Brown A. G. A., Vallenari A., Prusti T., de Bruijne J. H. J., Babusiaux C., Bailer-Jones C. A. L., 2018, *ArXiv e-prints*
- Gaustad J. E., McCullough P. R., Rosing W., Van Buren D., 2001, *PASP*, 113, 1326
- Ginsburg A., Mirocha J., , 2011, *PySpecKit: Python Spectroscopic Toolkit, Astrophysics Source Code Library*
- Gordon K. D., Clayton G. C., Misselt K. A., Landolt A. U., Wolff M. J., 2003, *The Astrophysical Journal*, 594, 279
- Hainich R., Rühling U., Todt H., Oskinova L. M., Liermann A., Gräfener G., Foellmi C., Schnurr O., Hamann W.-R., 2014, *Astronomy & Astrophysics*, 565, A27
- Imara N., Blitz L., 2007, *The Astrophysical Journal*, 662, 969
- Israel F. P., de Graauw T., van de Stadt H., de Vries C. P., 1986, *The Astrophysical Journal*, 303, 186
- Kehrig C., Vílchez J. M., Pérez-Montero E., Iglesias-Páramo J., Hernández-Fernández J. D., Duarte Puertas S., Brinchmann J., Durret F., Kunth D., 2016, *Monthly Notices of the Royal Astronomical Society*, 459, 2992
- Kennicutt Jr. R. C., 1998, *The Astrophysical Journal*, 498, 541
- Kerton C. R., Ballantyne D. R., Martin P. G., 1999, *The Astronomical Journal*, 117, 2485
- Kim S., Staveley-Smith L., Dopita M. A., Freeman K. C., Sault R. J., Kesteven M. J., McConnell D., 1998, *The Astrophysical Journal*, 503, 674
- Krumholz M. R., Bate M. R., Arce H. G., Dale J. E., Guter-muth R., Klein R. I., Li Z.-Y., Nakamura F., Zhang Q., 2014, *Protostars and Planets VI*, pp 243–266
- Krumholz M. R., Burkhardt B., 2016, *Monthly Notices of the Royal Astronomical Society*, 458, 1671
- Lin Z., Hu N., Kong X., Gao Y., Zou H., Wang E., Cheng F., Fang G., Lin L., Wang J., 2017, *The Astrophysical Journal*, 842, 97
- Lopez L. A., Krumholz M. R., Bolatto A. D., Prochaska J. X., Ramirez-Ruiz E., 2011, *The Astrophysical Journal*, 731, 91
- Lopez L. A., Krumholz M. R., Bolatto A. D., Prochaska J. X., Ramirez-Ruiz E., Castro D., 2014, *The Astrophysical Journal*, 795, 121
- Lucke P. B., Hodge P. W., 1970, *The Astronomical Journal*, 75, 171
- Luridiana V., Morisset C., Shaw R. A., 2015, *Astronomy & Astrophysics*, 573, A42
- Marcolino W. L. F., Bouret J.-C., Martins F., Hillier D. J., Lanz T., Escolano C., 2009, *Astronomy & Astrophysics*, 498, 837
- Marino R. A., Rosales-Ortega F. F., Sánchez S. F., et al., 2013, *Astronomy & Astrophysics*, 559, A114
- Martins F., Schaerer D., Hillier D. J., 2005, *Astronomy & Astrophysics*, 436, 1049
- Massa D., Fullerton A. W., Sonneborn G., Hutchings J. B., 2003, *The Astrophysical Journal*, 586, 996
- Massey P., Lang C. C., Degioia-Eastwood K., Garmany C. D., 1995, *The Astrophysical Journal*, 438, 188
- Massey P., Silkey M., Garmany C. D., Degioia-Eastwood K., 1989, *The Astronomical Journal*, 97, 107
- McCall M. L., 1984, *Monthly Notices of the Royal Astronomical Society*, 208, 253
- McKee C. F., Williams J. P., 1997, *The Astrophysical Journal*, 476, 144
- McLeod A. F., Dale J. E., Ginsburg A., Ercolano B., Gritschneider M., Ramsay S., Testi L., 2015, *Monthly Notices of the Royal Astronomical Society*, 450, 1057
- McLeod A. F., et al., 2016a, *Monthly Notices of the Royal Astronomical Society*, 455, 4057
- McLeod A. F., et al., 2016b, *Monthly Notices of the Royal Astronomical Society*, 462, 3537
- McLeod A. F., Reiter M., Kuiper R., Klaassen P. D., Evans C. J., 2018, *Nature*, 554, 334
- Mokiem M. R., de Koter A., Vink J. S., Puls J., Evans C. J., Smartt S. J., Crowther P. A., Herrero A., Langer N., Lennon D. J., Najarro F., Villamariz M. R., 2007, *Astronomy & Astrophysics*, 473, 603
- Monreal-Ibero A., Relaño M., Kehrig C., Pérez-Montero E., Vílchez J. M., Kelz A., Roth M. M., Streicher O., 2011, *Monthly Notices of the Royal Astronomical Society*, 413, 2242
- Monreal-Ibero A., Walsh J. R., Vílchez J. M., 2012, *Astronomy & Astrophysics*, 544, A60
- Mujres L. E., Vink J. S., de Koter A., Müller P. E., Langer N., 2012, *Astronomy & Astrophysics*, 537, A37
- Nazé Y., Chu Y.-H., Guerrero M. A., Oey M. S., Gruendl R. A., Smith R. C., 2002, *The Astronomical Journal*, 124, 3325
- Nazé Y., Chu Y.-H., Points S. D., Danforth C. W., Rosado M., Chen C.-H. R., 2001, *The Astronomical Journal*, 122, 921
- Niederhofer F., Hilker M., Bastian N., Ercolano B., 2016, *Astronomy & Astrophysics*, 592, A47
- Ochsendorf B. B., Zinnecker H., Nayak O., Bally J., Meixner M., Jones O. C., Indebetouw R., Rahman M., 2017, *Nature Astronomy*, 1, 784
- Oey M. S., 1996a, *The Astrophysical Journal*, 465, 231
- Oey M. S., 1996b, *The Astrophysical Journal*, 467, 666
- Oey M. S., 1996c, *The Astrophysical Journal Supplement*, 104, 71
- Oey M. S., Massey P., 1994, *The Astrophysical Journal*, 425, 635
- Oey M. S., Massey P., 1995, *The Astrophysical Journal*, 452, 210
- Osterbrock D. E., Ferland G. J., 2006, *Astrophysics of gaseous nebulae and active galactic nuclei*
- Ostriker E. C., McKee C. F., Leroy A. K., 2010, *The Astrophysical Journal*, 721, 975
- Pagel B. E. J., Edmunds M. G., Blackwell D. E., Chun M. S., Smith G., 1979, *Monthly Notices of the Royal Astronomical Society*, 189, 95
- Peimbert M., Peimbert A., Delgado-Inglada G., 2017, *PASP*, 129, 082001
- Pellegrini E. W., Baldwin J. A., Brogan C. L., Hanson M. M., Abel N. P., Ferland G. J., Nemala H. B., Shaw G., Troland T. H., 2007, *The Astrophysical Journal*, 658, 1119
- Pellegrini E. W., Baldwin J. A., Ferland G. J., 2010, *The Astrophysical Journal Supplement*, 191, 160

Pellegrini E. W., Baldwin J. A., Ferland G. J., 2011, *The Astrophysical Journal*, 738, 34

Pellegrini E. W., Oey M. S., Winkler P. F., Points S. D., Smith R. C., Jaskot A. E., Zastrow J., 2012, *The Astrophysical Journal*, 755, 40

Pérez-Montero E., 2017, *PASP*, 129, 043001

Pettini M., Pagel B. E. J., 2004, *Monthly Notices of the Royal Astronomical Society*, 348, L59

Pilyugin L. S., Grebel E. K., 2016, *Monthly Notices of the Royal Astronomical Society*, 457, 3678

Pilyugin L. S., Grebel E. K., Mattsson L., 2012, *Monthly Notices of the Royal Astronomical Society*, 424, 2316

Rahner D., Pellegrini E. W., Glover S. C. O., Klessen R. S., 2017, *Monthly Notices of the Royal Astronomical Society*, 470, 4453

Relaño M., Beckman J. E., 2005, *Astronomy & Astrophysics*, 430, 911

Relaño M., Monreal-Ibero A., Vílchez J. M., Kennicutt R. C., 2010, *Monthly Notices of the Royal Astronomical Society*, 402, 1635

Roman-Duval J., Gordon K. D., Meixner M., Bot C., Bolatto A., et al., 2014, *The Astrophysical Journal*, 797, 86

Rousseau J., Martin N., Prévot L., Rebeirot E., Robin A., Brunet J. P., 1978, *A&AS*, 31, 243

Russell S. C., Dopita M. A., 1992, *The Astrophysical Journal*, 384, 508

Schaye J., Crain R. A., Bower R. G., Furlong M., Schaller M., Theuns T., Dalla Vecchia C., Frenk C. S., et al., 2015, *Monthly Notices of the Royal Astronomical Society*, 446, 521

Skiff B. A., 2014, *VizieR Online Data Catalog*

Smith L. J., Norris R. P. F., Crowther P. A., 2002, *Monthly Notices of the Royal Astronomical Society*, 337, 1309

Smith Neubig M. M., Bruhweiler F. C., 1999, *The Astronomical Journal*, 117, 2856

Sternberg A., Hoffmann T. L., Pauldrach A. W. A., 2003, *The Astrophysical Journal*, 599, 1333

Tielens A. G. G. M., 2005, *The Physics and Chemistry of the Interstellar Medium*

Toribio San Cipriano L., Domínguez-Guzmán G., Esteban C., García-Rojas J., Mesa-Delgado A., Bresolin F., Rodríguez M., Simón-Díaz S., 2017, *Monthly Notices of the Royal Astronomical Society*, 467, 3759

Vink J. S., de Koter A., Lamers H. J. G. L. M., 2001, *Astronomy & Astrophysics*, 369, 574

Vogelsberger M., Genel S., Springel V., Torrey P., Sijacki D., Xu D., Snyder G., Bird S., Nelson D., Hernquist L., 2014, *Nature*, 509, 177

Weaver R., McCray R., Castor J., Shapiro P., Moore R., 1977, *The Astrophysical Journal*, 218, 377

Wegner W., 2006, *Monthly Notices of the Royal Astronomical Society*, 371, 185

Weilbacher P. M., Monreal-Ibero A., Kollatschny W., Ginsburg A., McLeod A. F., Kamann et al., 2015, *Astronomy & Astrophysics*, 582, A114

Weilbacher P. M., Streicher O., Urrutia T., Jarno A., Pécontal-Rousset A., Bacon R., Böhm P., 2012, in *Society of Photo-Optical Instrumentation Engineers (SPIE) Conference Series Vol. 8451 of Society of Photo-Optical Instrumentation Engineers (SPIE) Conference Series, Design and capabilities of the MUSE data reduction software and pipeline*. p. 0

Westmoquette M. S., James B., Monreal-Ibero A., Walsh J. R., 2013, *Astronomy & Astrophysics*, 550, A88

Will J.-M., Bomans D. J., Dieball A., 1997, *A&AS*, 123, 455

Wong T., Hughes A., Ott J., Muller E., Pineda J. L., Bernard J.-P., Chu Y.-H., Fukui Y., Gruendl R. A., Henkel C., Kawamura A., Klein U., Looney L. W., Maddison S., Mizuno Y., Paradis D., Seale J., Welty D. E., 2011, *The Astrophysical Journal Supplement*, 197, 16

Zaritsky D., Harris J., Thompson I. B., Grebel E. K., 2004, *The*

Astronomical Journal, 128, 1606

APPENDIX A: UNCERTAINTY ESTIMATION

In this section we briefly describe the source of uncertainties for the different quantities computed in this paper.

- (i) **Luminosity of the ionised gas $L(\text{H}\alpha)$.** The $\text{H}\alpha$ luminosity within a given radius is computed from the $\text{H}\alpha$ flux measured within the same radius, assuming a distance of 50 kpc to the LMC. The flux measurement is made from the extinction-corrected and continuum-subtracted $\text{H}\alpha$ emission line map. Given the good agreement between the MUSE and SHASSA $\text{H}\alpha$ fluxes (see main text), we compute $L(\text{H}\alpha)$ by assuming a generous $\pm 10\%$ uncertainty on the measured flux. This is propagated to $Q(\text{H}\alpha)$ and P_{dir} .
- (ii) **Photon flux Q_0 .** to convert the spectral type and luminosity class of the classified O-type stars we rely on the stellar parameters derived in [Martins et al. \(2005\)](#). The main source of uncertainty for the photon flux is therefore the fact that these authors use solar metallicity. In lower-metallicity environment such as the LMC, stars are hotter and Lyman continuum fluxes are higher ([Smith et al. 2002](#)), but a similar set of calculations/calibrations are unavailable at present. The used photon fluxes are therefore most probably underestimated, and the derived f_{esc} a lower limit.
- (iii) **Electron densities.** These two quantities are measured from the n_e and v_r maps from circular apertures centred on the regions of interest. The uncertainties stated in Table 5 correspond to the standard deviation measured for each circular extraction. These are propagated to P_{ion} , L_w and P_w .

APPENDIX B: STELLAR SPECTRA

Spectra of the identified O-type stars in N44 (Figures B1 and B2) and N180 (Figures B3, B4 and B5). See main text Section 3.

APPENDIX C: WIND LUMINOSITIES

We compute wind luminosities as expected from the spectral types of the stellar population within the single subregions according to model parameters given in [Muijres et al. \(2012\)](#). For a given spectral type, the mass-loss rate and terminal velocity used to determine the wind luminosity are listed in Table C1, where terminal velocities are 2.6 times the escape velocity.

APPENDIX D: RADIAL INTENSITY PROFILES

Sizes are determined as the radii encompassing 90% of the measured $\text{H}\alpha$ flux. Radial profiles are shown in Figures D1 and D2.

This paper has been typeset from a $\text{T}_{\text{E}}\text{X}/\text{L}^{\text{A}}\text{T}_{\text{E}}\text{X}$ file prepared by the author.

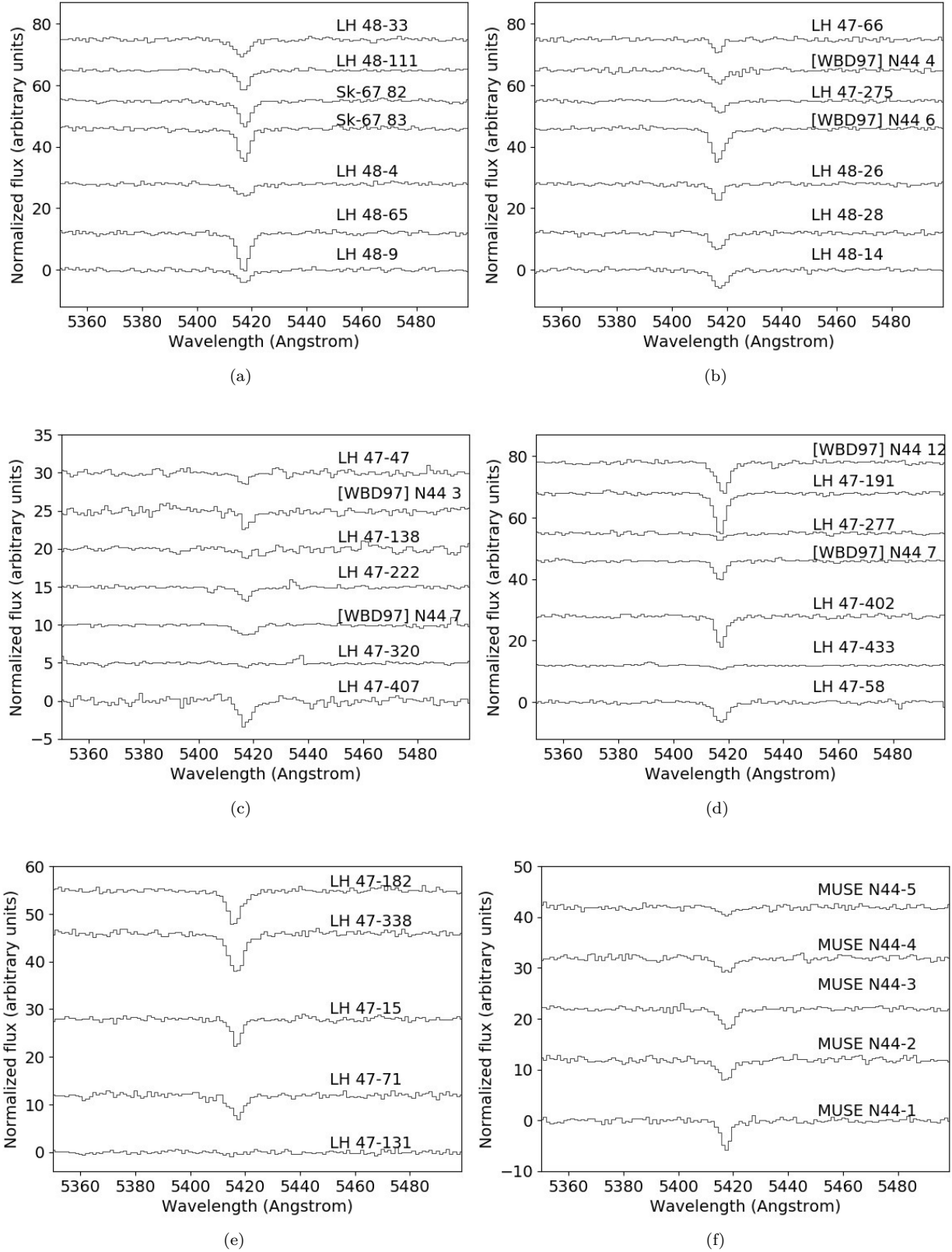


Figure B1. HeII line of the O-type stars in N44. All detected lines have at least 2 data points above 3.5 times the noise.

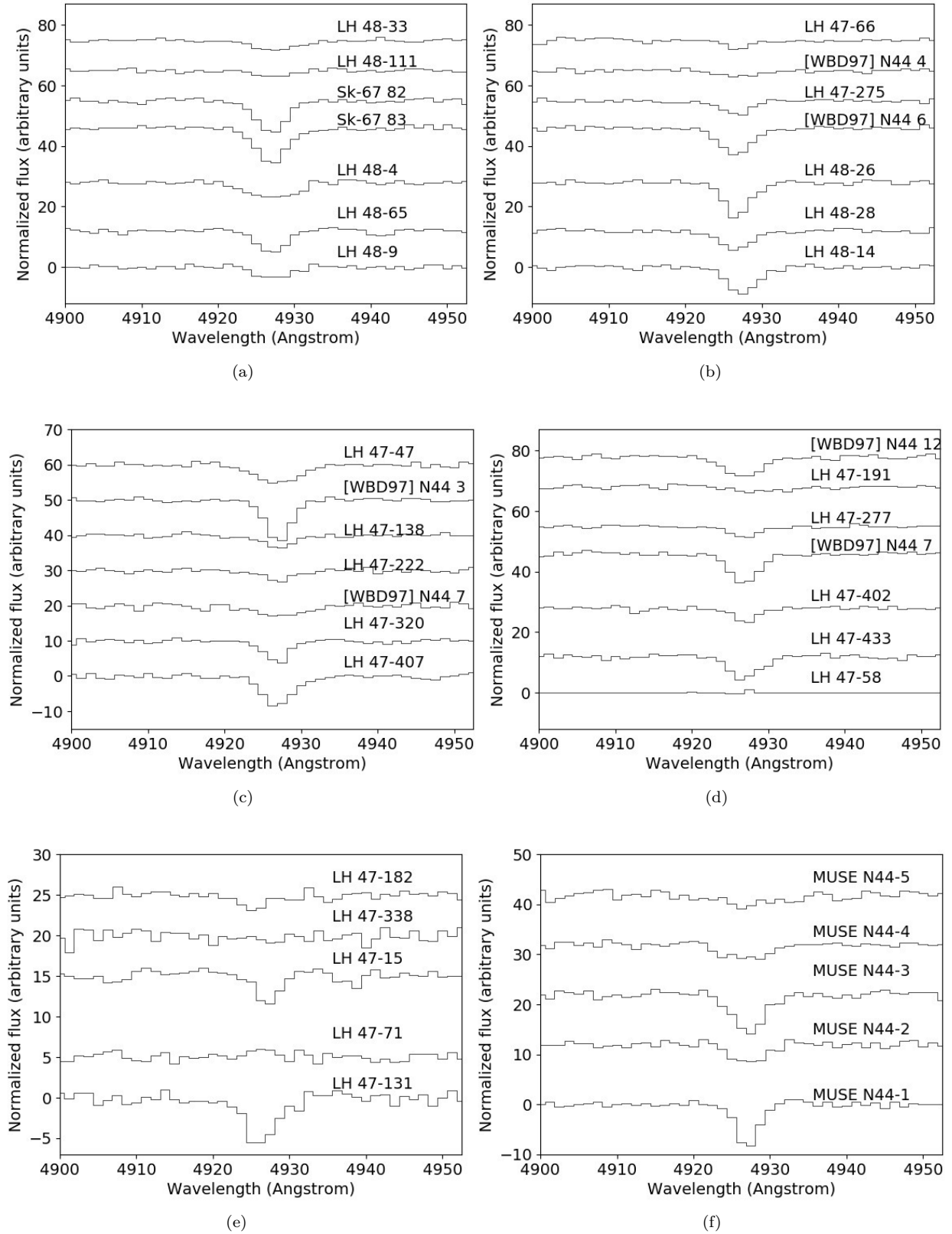


Figure B2. He I line of the O-type stars in N44.

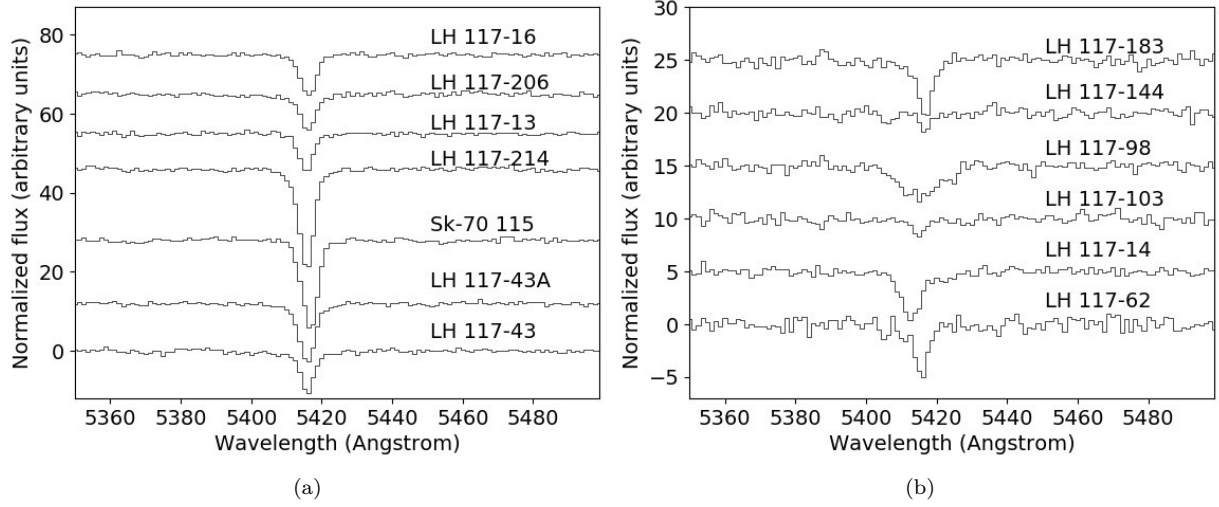


Figure B3. HeII line of the 13 O-type stars in N180 main. All detected lines have at least 2 data points above 3.5 times the noise.

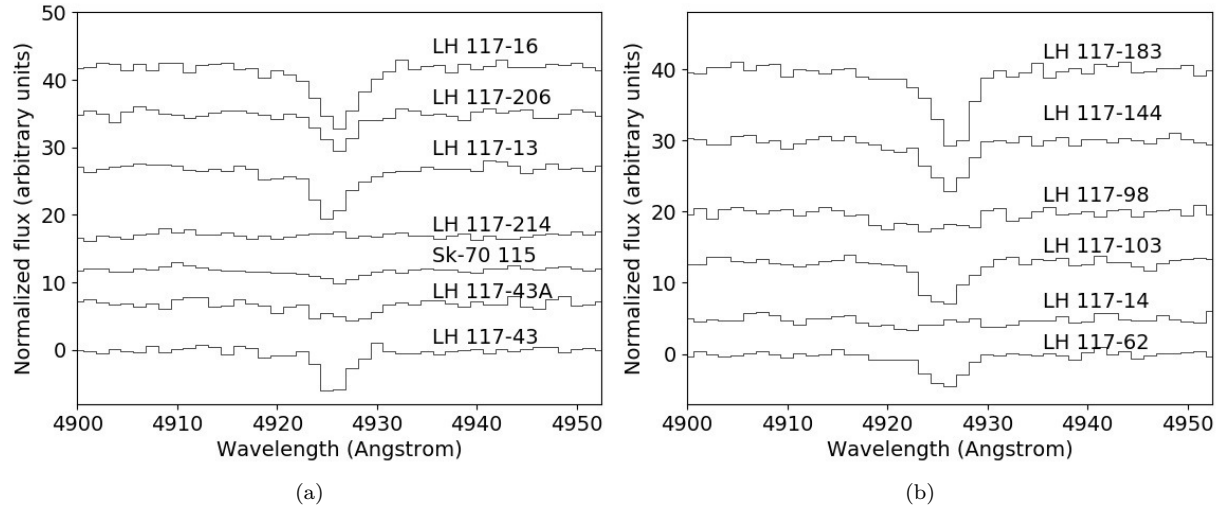


Figure B4. He I line of the N180 main O-type stars.

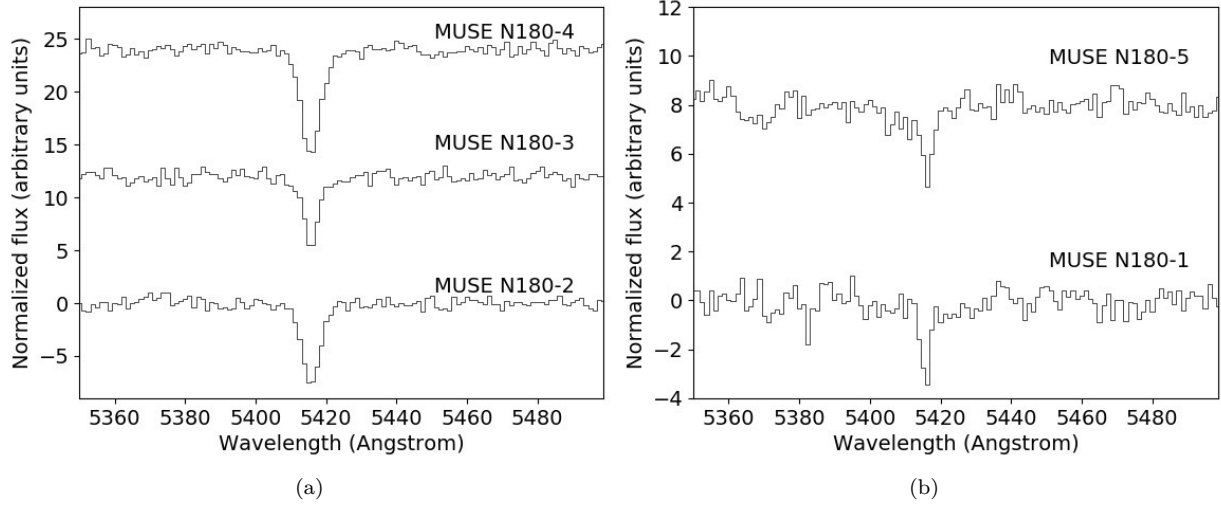


Figure B5. HeII line of the newly identified O-type stars in N180. All detected lines have at least 2 data points above 3.5 times the noise.

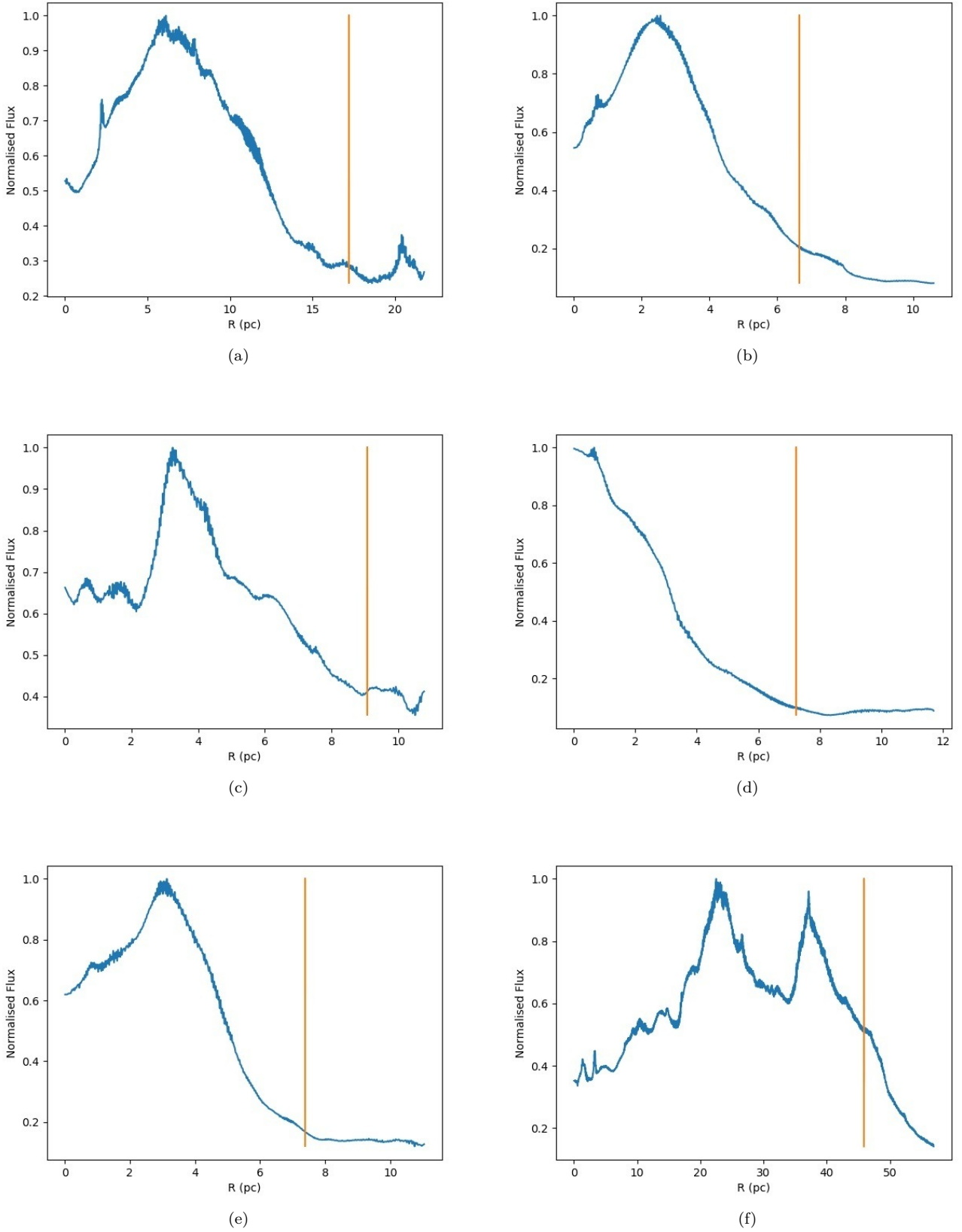


Figure D1. Radial intensity profiles for N44 A (a), N44 B (b), N44 B1 (c) N44C (d), N44 D (e) and N44 main (f). Vertical lines indicate the radius which encompasses 90% of the measured flux.

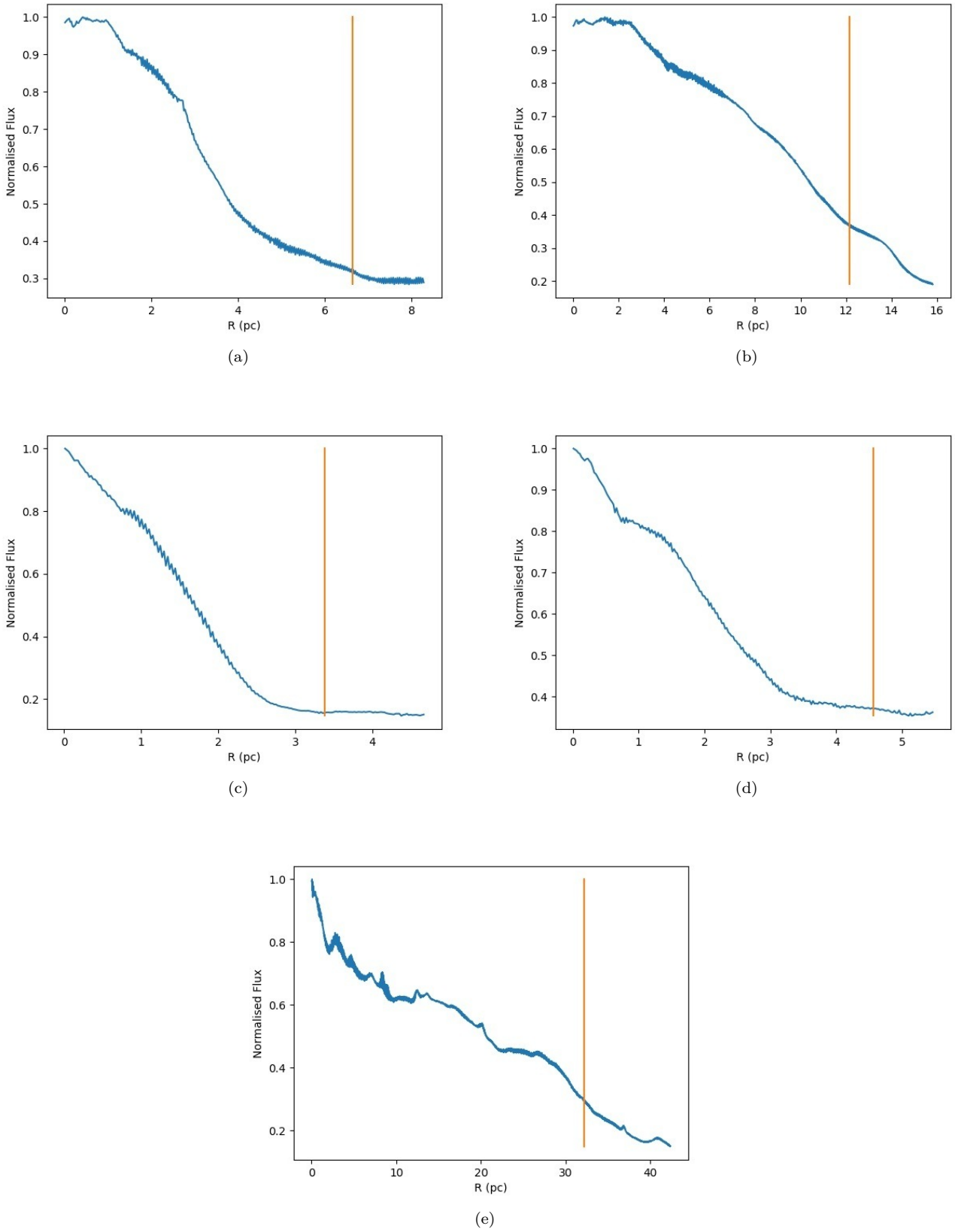


Figure D2. Radial intensity profiles for N180 A (a), N180 B (b), N180C (c) and N180 main (e). Vertical lines indicate the radius which encompasses 90% of the measured flux.

Spectral type	$\log(M)$ M_{\odot}/yr	v_{∞} km s^{-1}	$\log(L_{w,*})$ erg s^{-1}
O3 V	-5.375	2740.4	37.00
O5 III	-5.491	2176.2	36.68
O5 V	-5.829	2579.2	36.49
O6.5 III	-5.902	2106.0	36.24
O6.5 V	-6.427	2555.8	35.89
O7 III	-6.016	2074.8	36.12
O7 V	-6.624	2527.2	35.68
O 7.5 I	-5.642	1859.0	36.39
O7.5 V	-6.820	2493.4	35.47
O8 III	-6.286	1996.8	35.81
O8 V	-7.019	2454.4	35.26
O8.5 III	-6.409	1947.4	35.67
O8.5 V	-7.167	2399.8	35.09
O9 V	-7.374	2360.8	34.87
O9.5 I	-6.148	1593.8	35.57
O9.5 III	-6.646	1843.3	35.38
O9.5 V	-7.590	2319.2	34.64
B0.5 III	-6.900	1500	34.95

Table C1: Mass-loss rates (column 2) and terminal velocities (column 3) from [Muijres et al. \(2012\)](#) used to derive the wind luminosity for a fixed spectral type (column 4).